parameters of K = 20, L = 20 (Vijayakumar et al., 2007). Furthermore, Vesanto and Alhoniemi who reported two-level clustering suggested that the number of protoclusters N was determined as $N = k_{max}^2$, where k_{max} was an estimated maximum number of clusters (Vesanto and Alhoniemi, 2000). Because we predefined k = 20 from the viewpoint of a pathological estimation, the number of protoclusters was 400 according to the formula. According to the previous report and formula, we think the 20 × 20 matrix may be acceptable. Chavez-Alvarez et al. reported that the neighbourhood function was Gaussian with an initial radius ($\sigma_{initial}$) of 3.0 when K = 20 and L = 20 in their study (Chavez-Alvarez et al., 2014). To determine a final radius (σ_{final}), we tested BLSOM with a set of parameters (0.01, 0.05, 0.1, 0.25, 0.5, 1, 2, 3) according to the previous study (Ehsani and Quiel, 2008). Lower final radius than 2.0 could cause stepping-stone like clusters by the KM++ with k = 20, which was the maximum number in the study, partly because of overfitting. Therefore, we finally applied σ_{final} = 2.0, which did not cause any stepping-stone like clusters. As to τ, the number of total iterations of SOM, some previous neuroimaging studies applied 100 iterations for SOM and suggested that 100 iterations were sufficient to establish convergence of SOM, and, therefore we followed them (Peltier et al., 2003; Liao et al., 2008). We have implemented BLSOM software (in-house developed products) developed in C++.

One of the greatest advantages of SOM is the powerful visualization (Vesanto and Alhoniemi, 2000), which enables SOM to be suited for data understanding or survey. There are two common methods to visualize the results of SOM, U-Matrix and Component Planes. Especially, the Component Planes can show the information of each parameter in each map unit and associations between clusters and variables (Alhoniemi et al., 1999). We used the Component Planes to visualize the relation between variables of each DTI-based parameter clearly. Using the Component Planes, SOM may allow us to evaluate the classification options different from a fixed diagnosis (Wang et al., 2002).

2.6. Unsupervised clustering: KM clustering

The KM algorithm is a classic statistical clustering method (MacQueen, 1967) computed in an off-line mode and does not perform competitive learning as does SOM. Its objective, for K clusters, is to iteratively minimize the within-class inertia by assigning the feature vectors to the nearest cluster centre and update its value. The number of clusters has to be determined prior to calculation.

The algorithm of the standard KM is as follows:

1 Start by initializing C that will contain K cluster centres $c_k \in \mathbb{R}^d$ such that $1 \leq K \leq N$. The set $C = \{c_1, c_2, ..., c_k\}$ will be initialized with the vectors x_j randomly chosen from the data set $X \subset \mathbb{R}^i$.
2 Assign each vector x_j from the data set to the nearest centre c_k using the Euclidean distance metric, $d(x_j, c_k) = \|x_j - c_k\|$.
3 Update the new cluster centres c_k with the average value of its members by $c_k = (1/C_k) \sum_{x_j \in C_k} x_j$, where C_k represents the number of elements in the respective cluster.
4 Repeat steps 2 and 3 if any partition was modified since last iteration.

Although the procedure will always terminate, the standard KM might converge to a local minimum because it uses vectors chosen at random from the data set to initialize the clusters. Therefore, we used a modified version of KM, called the K-means++ (KM++) algorithm (Arthur and Vassilvitskii, 2007), that chooses centres at random from the data points but weighs the data points according to their squared distance from the closest centre already chosen. The KM++ algorithm shows drastic improvement in both speed and accuracy compared with the classic algorithm. The KM++ algorithm is defined as follows:

1a Take one centre c_1, chosen uniformly at random from X.
1b Take a new centre c_i, choosing $x \in X$ with probability $D(x)^2 / \sum_{x \in X} D(x)^2$

1c Repeat step 1b until we have taken K centres altogether.
2–4. Proceed as with the standard KM algorithm.

In addition to KM++, we repeated KM++ trials and selected the best cluster among different clusters from multiple KM++ trials by the silhouette index (Rousseeuw, 1987). It calculates the silhouette index for each datum, average silhouette index for each cluster and overall average silhouette index for the total data set. Using the method, each cluster could be represented by so-called silhouette, which is based on the comparison of its tightness and separation. The average silhouette index can be applied for evaluation of clustering validity. The overall average silhouette index (SI) is defined by $SI = (1/K) \sum_{j=1}^{K} S_j$, where S_j is a silhouette local coefficient defined by $S_j = (1/n_j) \sum_{i=1}^{n_j} s_i$, where s_i is a silhouette index for the i-th object defined by $s_i = (b_i - a_i)/max(b_i, a_i)$, where a_i is the mean distance between object i and objects of the same class j and b_i is the minimum mean distance between object i and objects in class closest to class j. In the study, 1000 KM++ trials were performed in each K. We have little prior knowledge about the number of K, and it can differ according to what users want to know (e.g. tumour detection, tumour grading or outcome prediction) using the clustered images. In the present study, we empirically chose the numbers of K = 4, 6, 8, 10, 12, 16, 20 according to the number of estimated segmentations in the abnormal brain with a glioma. We implemented these algorithms in the in-house SOM software, which enabled the use of BLSOM followed by KM++.

2.7. Diffusion tensor-based clustered image (DTcI)

After unsupervised clustering by BLSOM followed by KM++, 400 protoclusters (weighted vectors) with K-class label information were generated. Label information of the nearest protocluster using the Euclidean distance metric was assigned to each voxel on the seven intensity-normalized diffusion tensor images within the binary mask image from FSL's BET. Finally, voxel-based images with K-class label information were obtained. We called them DTcIs (Fig. 1). Using the unsupervised clustering method, DTcIs can be easily obtained without any initial segmentation.

2.8. Classification using DTcI: definition of ROI

Gliomas generally show unclear and irregular boundaries with discontinuities and variety. ROIs were manually traced by two of the authors in the DTI space according to abnormalities on MP-RAGE, without any knowledge of the clinical or pathological data. It should be noted that ROIs were defined on the basis of abnormal signal intensities in MP-RAGE, which could include tumour as well as oedema, necrosis and cystic parts. For simplicity, we defined ROIs per four axial slices from the top slice of the abnormal regions and counted the total number of voxels in each patient. If the number of voxels was <400, we redefined ROIs per two axial slices to increase the number of total voxels. Finally, the number of voxels in each ROI ranged from 326 to 9316. We only used these ROIs for feature extraction for SVM as mentioned in the next subsection.

2.9. Classification using DTcI: feature extraction for tumour grading

The ratio of each class in DTcIs was calculated from ROIs in each subject. Then, the common logarithmic value of the ratio was calculated by $log_{10}(p + 10^{-2})$, where p is a ratio of each class (%) and used for input features to SVM. The features were defined as log-ratio values according to $U = \{x_i \in \mathbb{R}^K, 1 \leq i \leq N\}$, where N is the number of subjects (Fig. 1).

2.9.1. Classification using DTcI: SVM
SVM (Vapnik, 1998) is a widely used method because of its remarkable classification performance and the simplicity of its theory and

implementation. Accordingly, we chose a linear kernel SVM as a classifier to distinguish between LGGs and HGGs. The hyperparameter (C) of the linear kernel SVM was optimized by using a two-step grid-search technique with five-fold cross-validation according to the recommendation described in a practical guide to SVM classification (Hsu et al., 2003; Ota et al., 2014). First, the best value of C_{coarse} was found by a coarse grid-search on $\log_2 C = -5, -3, ..., 15$. Then, the best value of C_{fine} was obtained by a fine grid-search on $\log_2 C = C_{coarse} - 2, C_{coarse} - 1.75, ..., C_{coarse} + 1.75, C_{coarse} + 2$. The best C_{fine} was used to generate the final classifier for each training set.

A LOOCV strategy was used to assess the classification performance because the strategy is widely used in machine learning and allows using most of the data for training (Dosenbach et al., 2010). During LOOCV, each subject is designated as a test subject in turn, while the remaining subjects are used to train the SVM classifier. The decision function derived from the training subjects is then used to classify or calculate a decision value about the test subject. After all LOOCV repeats, the accuracy, sensitivity and specificity for all folds are averaged together to generate the final accuracy, sensitivity and specificity estimate. We also evaluated decision values (Chang and Lin, 2011) for receiver operating characteristic (ROC) curves and area under the curve (AUC). Furthermore, we repeated the LOOCV strategy 100 times to calculate confidence intervals (CIs) of these estimates.

We used C++ and the LIBSVM library (Chang and Lin, 2011; software available at http://www.csie.ntu.edu.tw/~cjlin/libsvm) to implement a linear kernel SVM with a two-step grid-search technique and a LOOCV strategy.

2.10. Statistical analysis

To determine if the classification performances were significantly different according to the number of K in the KM++ method ($K = 4, 6, 8, 10, 12, 16, 20$), we repeated the LOOCV strategy 100 times. AUCs in different K were then analysed by one-way ANOVA followed by Tukey's multiple comparison tests. Differences were considered significant for $p < 0.05$.

Then, to evaluate the behaviour of the classifier in the K-class that revealed the best classification performance, we used the pROC library for R to generate ROC curves with 95% CIs computed with 2000 stratified bootstrap replicates (Robin et al., 2011).

Wilcoxon–Mann–Whitney tests with exact p-values and CIs calculated by a permutation test were used to compare the log-ratio values of each class in the K class that revealed the best classification performance between the LGG and HGG groups (Hothorn et al., 2006). Because of the multiple comparisons in K classes, a Bonferroni correction for multiple comparisons was applied, and differences between the groups were considered to be significant at a level of $p < 0.05/K$.

The ratios of normalized intensities on the seven diffusion tensor images of each class in the K class that revealed the best classification performance were analysed with the bootstrapped 95% CIs. The statistical software package R version 3.0.2 (The R Foundation for Statistical Computing, http://www.r-project.org/) was used to perform all statistical analyses.

3. Results

3.1. Unsupervised clustering

Fig. 2 illustrates the Component Planes in seven DTI-based variables by the SOM analysis. Visual inspection of the SOM patterns demonstrated that the Component Planes of DWI and FA were obviously different from the others. Although general patterns of MD, S0, L1, L2 and L3 Component Planes seemed similar, the details among them differed. In the case of $K = 16$ (Fig. 2), for example, FA values in class number 13, DWI values in class number 15 and MD, S0, L1, L2 and L3 values in class number 4 were highest among all classes. SOM also showed that the DWI component of class numbers 1, 2, 9, 12 and 13 had variations from low to high values, and that the FA component of class numbers 9, 10, 12 and 14 had variations from low to high values. Class numbers 12, 13 and 16 in the L1 Component Plane were higher than those of the MD, S0, L2 and L3 Component Planes. Class numbers 2, 6, 7 and 8 in the MD, L1, L2 and L3 Component Planes were higher than
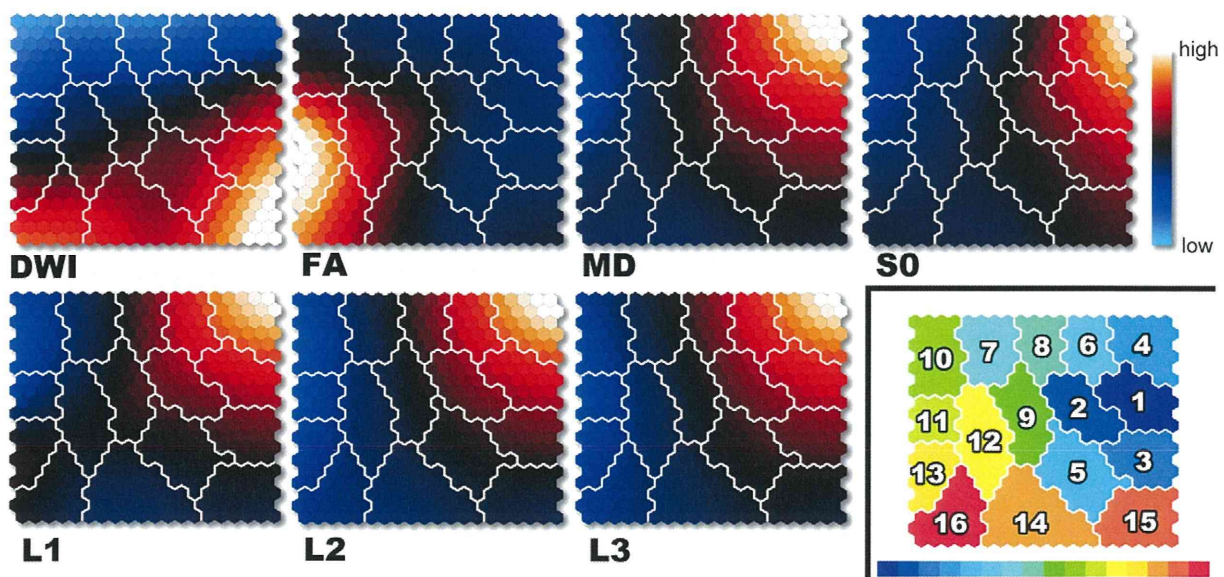

Fig. 2. Visualization of seven DTI-based variables on Component Planes with SOM. Each node (protocluster) is colorized from blue to red according to the intensities in each diffusion tensor image. The white lines between nodes denote inter-class borderlines obtained by KM++ with $K = 16$ on SOM. SOM component planes can help to interpret detailed intensity profiles or patterns in each diffusion tensor image (lower right). The 16-class cluster map on the 20 × 20 SOM. Each class number corresponds to intensity on DTI-based clustered images. DWI = diffusion-weighted imaging; FA = fractional anisotropy; L1 = first eigenvalue; L2 = second eigenvalue; L3 = third eigenvalue; MD = mean diffusivity; S0 = raw T2 signal without diffusion weighting.
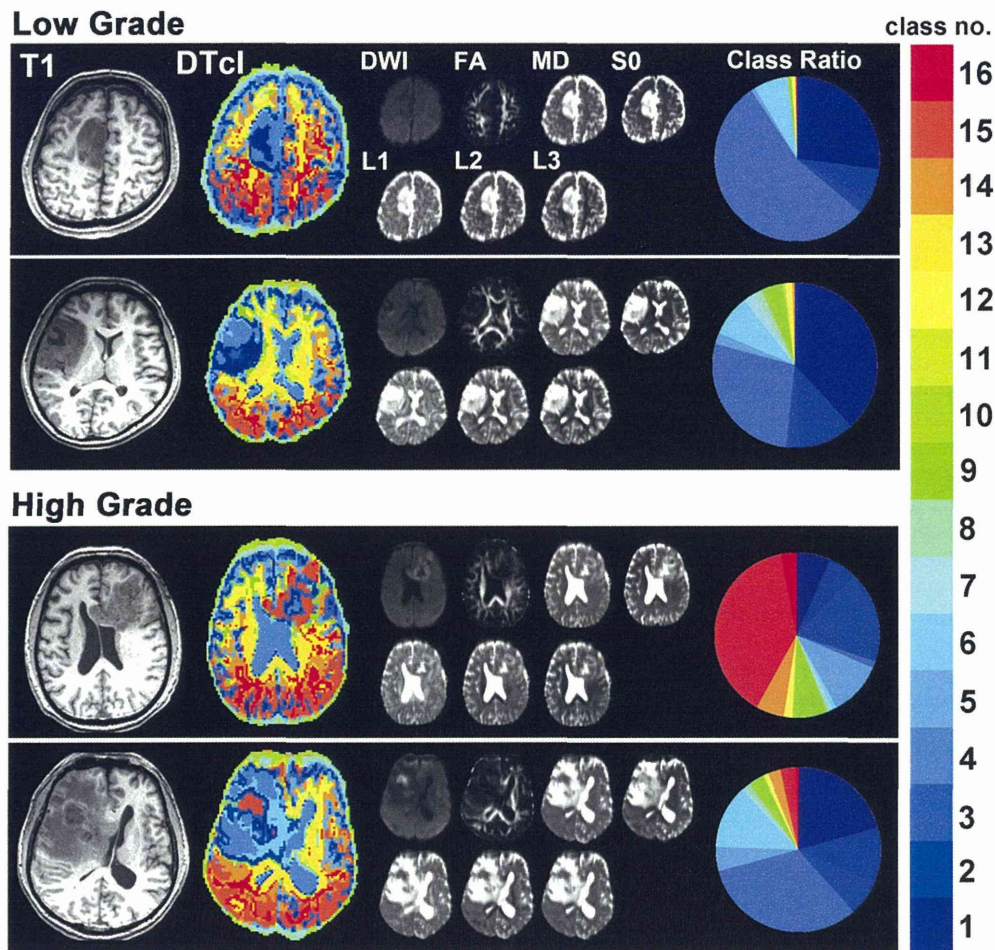
Fig. 3. The representative cases of low- (upper) and high- (lower) grade gliomas, including the 16-class DTcIs that showed the highest classification performance. The T1-weighted images, DTcIs, seven diffusion tensor images and the ratios in each class number are shown for each patient. DWI = diffusion-weighted imaging; FA = fractional anisotropy; L1 = first eigenvalue; L2 = second eigenvalue; L3 = third eigenvalue; MD = mean diffusivity; S0 = raw T2 signal without diffusion weighting. Each colour on DTcIs and circular charts correspond to each class number, shown in the colour bar.

those in the S0 Component Plane. Class number 9 in the MD and L1 Component Planes was higher than that in the S0, L2 and L3 Component Planes.
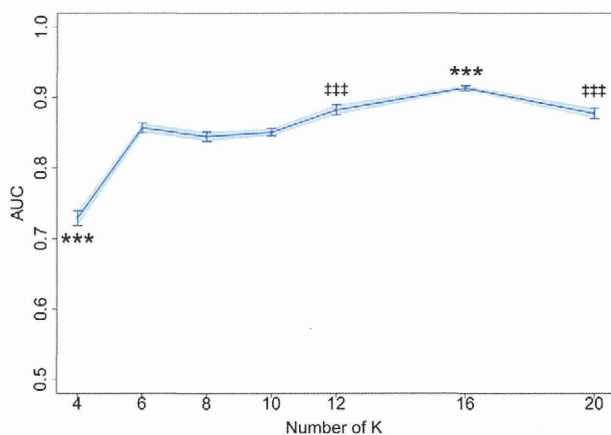

Fig. 4. Plots of AUC versus the number of K in the KM++ method. Values are means and error bars, and light blue shades represent 95% CIs. ***$p < 0.001$ (versus all the rest). ‡‡‡$p < 0.001$ (versus K = 4,6,8,10,16), one-way ANOVA followed by Tukey's multiple comparison tests. The 16-class diffusion tensor-based clustered images significantly showed the highest AUC (0.912; 95% CIs = 0.903–0.922).

Representative cases of LGGs and HGGs are shown in Fig. 3. Although the boundaries of LGGs could be clearly recognized, it was much difficult to recognize the boundaries of HGGs. Furthermore, DTcIs revealed few warm coloured classes, such as class numbers 14, 15 and 16 in LGGs, whereas there were more warm coloured classes in HGGs than in LGGs. Thus, the clear differentiations between LGGs and HGGs on DTcIs could be visually recognized.

3.2. SVM classification using DTcI

The performances of LOOCV using DTcI and SVM are shown in Fig. 4. The differences in AUCs were significant among the classes [$F(6, 693) = 246.1, p < 10^{-168}, \eta_p^2 = 0.68$]. Tukey's post-hoc tests showed that AUC was significantly higher for the 16-class DTcIs than for others ($p < 0.001$). The tests also showed that AUCs were significantly higher for the 12- and 20-class DTcIs than for the 4-, 6-, 8- and 10-class DTcIs ($p < 0.001$). There were no significant differences in AUCs between the 12-class and 20-class DTcIs. The tests also showed that AUC was significantly lower for the 4-class DTcIs than for the others ($p < 0.001$). AUC of the 16-class DTcIs was the highest among classes (0.912; 95% CI = 0.903–0.922) (Fig. 5). The sensitivity, specificity and accuracy of the 16-class DTcIs were 0.848 (95% CI = 0.845–0.852), 0.745 (95% CI = 0.733–0.757) and 0.804 (95% CI = 0.800–0.809), respectively. In contrast, AUC of the 4-class DTcIs was the lowest (0.729; 95% CI = 0.718–0.739). There were no significant group differences in AUCs between in the 6-, 8- and 10-class DTcIs (0.856, 0.844 and 0.850, respectively).
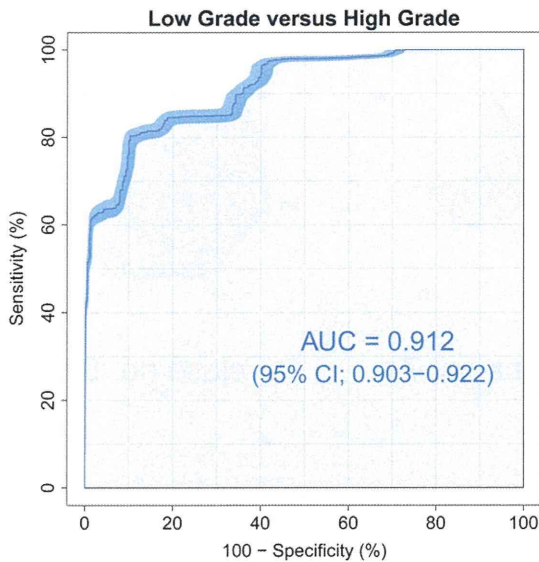
Fig. 5. ROC curves (dark blue line), with AUC and 95% CIs shown in blue shades surrounding the dark blue line, for differentiating high-grade from low-grade gliomas by using the 16-class diffusion tensor-based clustered images.

3.3. Differences in log-ratio values

The log-ratio values of each class of the 16-class DTcIs that had the highest classification performance were compared between LGGs and HGGs (Fig. 6). The values of class numbers 14, 15 and 16 were significantly higher in HGGs than in LGGs ($p < 0.005$, r = 0.52; $p < 0.001$, r = 0.60; $p < 0.001$, r = 0.73; respectively). The values of class numbers 12 and 13 also revealed higher trends in HGGs ($p < 0.01$, r = 0.48; $p < 0.01$, r = 0.50; respectively).

3.4. Ratio of DTI-based parameters

The ratios of normalized intensities of the seven diffusion tensor images for each class number in the 16-class DTcIs that revealed the highest classification performance are shown in Fig. 7.

As mentioned above, the ratios of class numbers 14, 15 and 16 were significantly higher in HGGs than in LGGs. The chart patterns of class numbers 14 and 15 seemed similar and comprised high DWI values and low FA values. Class number 15 had the highest DWI values among all. In FA, class number 14 had higher values than class number 15. The variables of class number 16 comprised high FA and DWI values and were different from those of class numbers 14 and 15. All three classes included low values in MD, S0, L1, L2 and L3. Although the variables of class numbers 3 and 5 included high DWI values and low values for

other features, there were no significant differences in the log-ratio values between LGGs and HGGs ($p = 0.28$, r = −0.19; $p = 0.84$, r = 0.03; respectively).

The indices of class numbers 12 and 13 also revealed higher trends in HGGs. The chart patterns of class numbers 12 and 13 were very different from those of class numbers 14, 15 and 16. The highest FA values were seen in class number 13. The variables of class numbers 12 and 13 included low DWI values. Low values in MD, S0, L1, L2 and L3 were seen in class numbers 12, 13, 14, 15 and 16.

4. Discussion

4.1. Study overview

In this study, we investigated a two-step procedure for predicting glioma grade. In the first step, the unsupervised clustering method with SOM followed by KM++ was used to obtain voxel-based DTcIs with multiple DTI-based parameters. DTcIs enabled visual grading of gliomas. In the second step, the validity of DTcIs for glioma grading was assessed in a supervised manner using SVM. The 16-class DTcIs revealed the highest classification performance for predicting the glioma grade. The sensitivity, specificity, accuracy and AUC of the 16-class DTcIs for differentiating HGGs and LGGs were 0.848, 0.745, 0.804 and 0.912, respectively. The classifier in the 16-class DTcIs showed that the ratios of class numbers 14, 15 and 16 were significantly higher and those of class numbers 12 and 13 showed higher trends in HGGs than in LGGs. Thus, these results indicate that our clustering method of seven parameters can be useful for determining glioma grade visually, despite not using a complicated combination of a high number of features from many modalities.

4.1.1. Clustering method

The two-level clustering approach was used in our study since it has the following two important benefits: noise reduction and computational cost. Because of the character of KM++ mentioned in the Materials and methods section, outliers extracted from DTI parameters can make its clustering accuracy worse. When BLSOM is applied prior to KM++, outliers can be filtered out and the clustering accuracy will be better. The AUC only with the KM++ algorithm without BLSOM was 0.646 with $K = 16$ and remarkably worse than that with the two-level clustering approach. Another important benefit is the reduction of the computational cost. In our study, the KM++ was repeated 1000 times to obtain more stable results. The computational time of the two-level clustering approach for 1000 KM++ trials was 210 s (204 s for BLSOM and 6 s for 1000 KM++ trials) for 117,232 input vectors in the study. On the other hand, the computational time only for the 1 KM++ trial without BLSOM was 305 s and around 85 hours for 1000 KM++ trials.
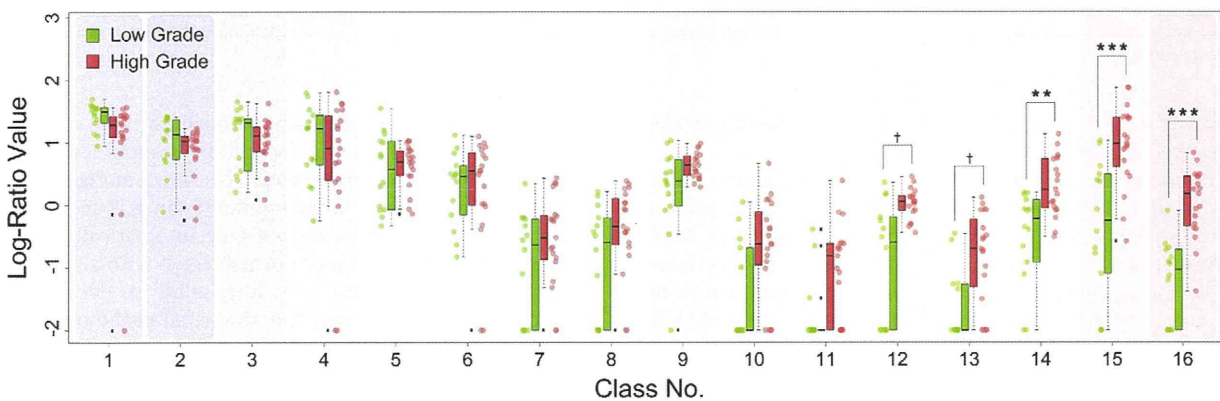

Fig. 6. Strip chart and box plots showing median, interquartile range, inner fence and outliers (○) for log-ratio values of each class by 16-class diffusion tensor-based clustered images in patients with low- (green) and high- (red) grade gliomas. ***$p < 0.001$, **$p < 0.005$, †$p < 0.01$ by exact Wilcoxon–Mann–Whitney rank sum tests.

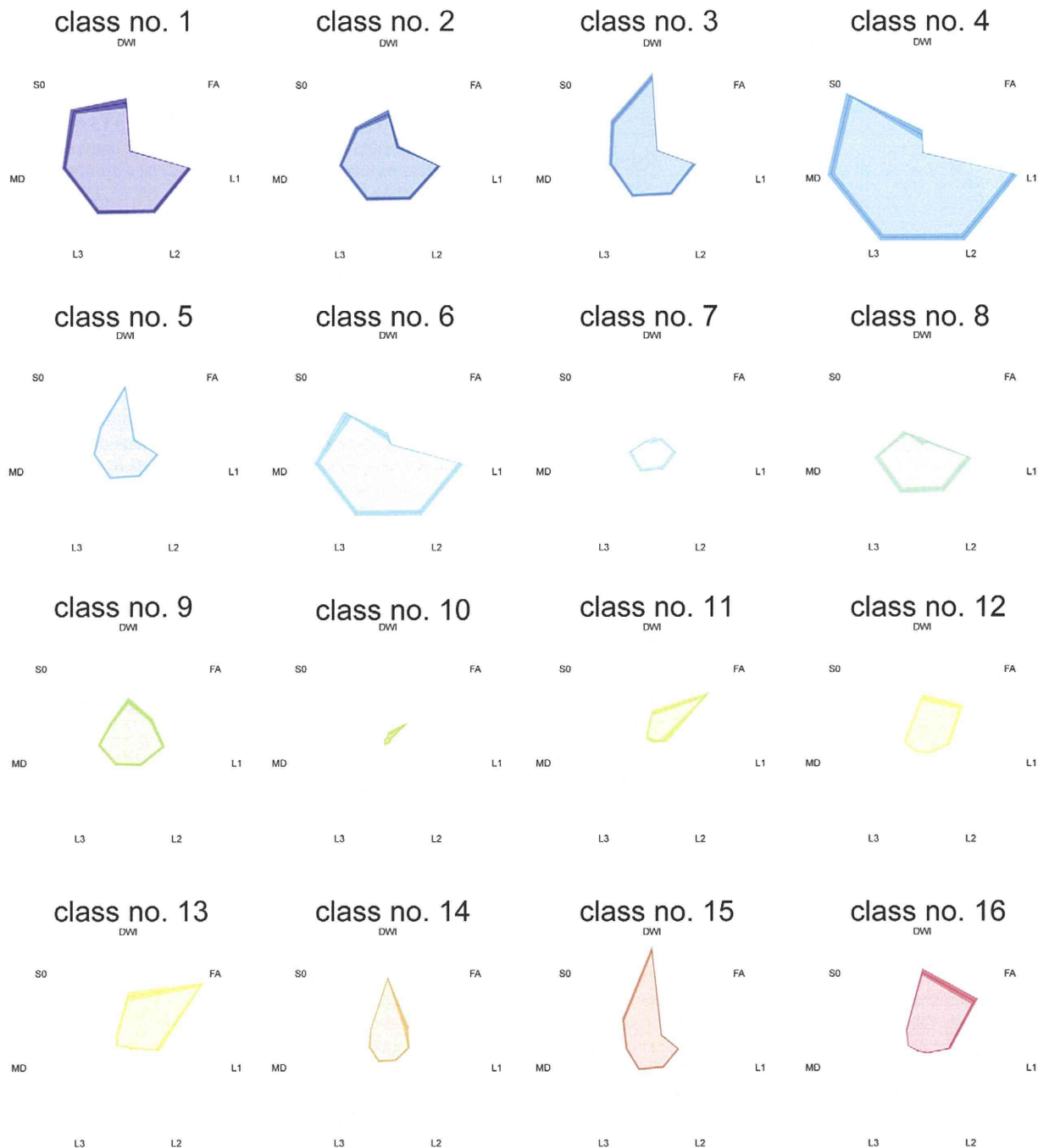**Fig. 7.** Radar charts of seven DTI-based variables in each class by 16-class diffusion tensor-based clustered images. Shades surrounding dark-coloured lines represent bootstrapped 95% CIs. DWI = diffusion-weighted imaging; FA = fractional anisotropy; L1 = first eigenvalue; L2 = second eigenvalue; L3 = third eigenvalue; MD = mean diffusivity; S0 = raw T2 signal without diffusion weighting.

For these facts, the two-level approach can be effective especially for clustering of a larger data set.

Deciding optimal parameters for SOM is not easy as previous studies mentioned in their studies. Although we applied most of the parameters according to previous studies (Vesanto and Alhoniemi, 2000; Vijayakumar et al., 2007; Ehsani and Quiel, 2008; Chavez-Alvarez et al., 2014) in the study, it remains unclear, as mentioned in the Materials and methods section, whether these parameters for SOM lead to the best performance or not. The parameters might be verified by undertaking a prospective, randomized controlled study.

Our segmentation method does not need any initial segmentation for defining tumour lesions because features were extracted from the whole brain. Indeed, the DTcIs can segment the brain as some parts of

normal and abnormal areas unintentionally, but the method does not need any initial segmentation for defining tumour lesions and it is an important advantage of unsupervised clustering methods. When defining tumour lesions as an initial segmentation, it is needed to draw regions of interest intentionally or decide automatically which voxel is tumour, oedema, necrosis or normal tissue with a supervised clustering method. However, it is impossible to decide the correct boundary between normal and abnormal pathology on MRI. The voxel out of the boundary may include tumour cells considered from the infiltrative nature of glioma, which may influence grading of gliomas. We think that clustering for images of gliomas without an initial segmentation is an indispensable advantage and our method can satisfy this point.

4.2. Number of classes in DTcIs

The 16-class DTcIs had the best classification performance between HGGs and LGGs in this study. It is assumed that brain tumour images can be segmented at least into four classes (white matter, grey matter, CSF and abnormality) (Rajini and Bhavani, 2012). Within abnormalities, they can be consisted of tumour cells (high/low), gliosis, oedema, necrosis, haemorrhage, and the mixed structure of some of them. Therefore, when we consider the combination of those, several kinds of classes may be reasonable. Furthermore, we found the same cluster in grey matter and in tumours. Class numbers 14–16 that had significantly higher HGG values were seen in grey matter and showed low MD values, which corresponded to increased cellularity (Lam et al., 2002; Kao et al., 2013). This finding may indicate high cellularity within tumour areas. However, it is difficult to say on the basis of our results which class would fit to what tissue. Pathological studies of each class in DTcIs by biopsy or resection could clarify the relationship.

4.3. Multiple parameters in DTI

We selected L1, L2 and L3, that are the basis of DTI-related parameters, in order to compare previous pathological studies using those parameters. We also selected DWI, FA, ADC and S0 that are familiar to neurosurgeons in order to compare previous studies that used one of those parameters as a single parameter for glioma grading. In the previous study, Griffith et al. researched the pathologies of MD [(L1 + L2 + L3)/3], L1 and radial diffusivity [(L2 + L3)/2] and compared each parameter. Although MD was calculated from L1, L2 and L3, they have different information at least from the viewpoint of pathology (Griffith et al., 2012). We therefore think that each parameter has an important role clinically and pathologically and selected these parameters in the study. Some previous studies used one parameter, especially ADC, for tumour grading. Although one study suggested that HGGs with lower ADC values corresponded to increased cellularity (Kao et al., 2013), another reported that there was no significant difference in ADC values between LGGs and HGGs (Lam et al., 2002). These studies suggest that differentiating glioma grade on the basis of only one parameter is difficult. In our study, we used seven DTI-based parameters, including DWI, FA, MD, S0, L1, L2 and L3, and the results suggested that the DTI-based multiple parameters were useful for predicting glioma grade. However, it remains unclear which parameters have the most influence on clustering tumours. We identified unique DWI and FA Component Planes that can be predictive of malignancy. A previous study revealed no significant differences in DWI between LGGs and HGGs and indicated that predicting tumour grade only by using DWI had a limitation (Kono et al., 2001). Class numbers 14, 15 and 16 that were significantly higher in HGGs showed similar DWI values but different patterns of values in other DTI-based parameters. In addition to the results, we also calculated the AUC if using the combination of only DWI and FA, only DWI and only FA. However, the AUC of two parameters of DWI and FA was 0.642, 0.645, and 0.637, respectively and they all were much lower than the AUC of seven parameters. The additional analyses also support the idea that combined multiple parameters could be useful for predicting the grade of gliomas. Conversely, although FA values of HGGs were higher than LGGs in a previous study (Kao et al., 2013), class numbers 14 and 15 showed low FA values. Although general patterns of MD, S0, L1, L2 and L3 Component Planes in SOM seemed similar, their subtle differences revealed by multi-variate pattern analysis may be important for predicting grade. In fact, a pathological study using MRI reported that higher astrocytosis correlated with higher ADC and L1 (Griffith et al., 2012). Most cases of reactive astrocytosis can be identified from the infiltrating edge of an astrocytoma (Ironside, 1994), and it may be difficult to distinguish diffuse astrocytoma from astrocytosis (Camelo-Piragua et al., 2011). Axonal damage and cellular infiltration led to a reduction of L1 (Boretius et al., 2012), and radial diffusivity [(L2 + L3)/2] has been proposed as a marker of demyelination (Klawiter et al., 2011). Furthermore, loss of oligodendrocytes

correlated with L2 and L3 but not L1 (Griffith et al., 2012). Although we extracted seven parameters from DTI, it remains unclear which combination of the parameters is the best or if additional parameters can increase the accuracy for glioma grading. Several features other than the seven parameters, for example, eigenvectors, might provide better results if included. Further studies are needed to assess which combination of parameters is best for glioma grading.

One of the limitations in our study was the influence of distortions on voxel-based clustering. Original DWIs for DTI were acquired by using EPI to reduce acquisition time and artefacts related to physiological motion. Unfortunately, this fast acquisition scheme is highly sensitive to eddy currents induced by the large diffusion gradients and to another distortion induced by susceptibility artefacts (Mangin et al., 2002). A prominent source of artefacts for EPI is the effect of inhomogeneities close to tissue–air and tissue–bone interfaces, such as those around the frontal sinus and petrous bone (Jezzard and Clare, 1999). To reduce artefacts by eddy currents, the data were corrected by using the FDT program (Smith et al., 2004). Furthermore, the FUGUE program was used to reduce susceptibility artefacts for EPI that depend on the subject's head geometry. Only DTI-based parameters were used for glioma grading in our study, although conventional MRI sequences, such as T1WI, T1WIce and T2WI, were scanned. The reason is that these conventional images are spatially different from DTI because of distortions. The differences require more accurate image registration between them for calculating voxel-based images. Multiple parameters of DTI-based parameters as well as conventional MRI parameters combined with an accurate registration algorithm may generate voxel-based clustered images that predict the grade of gliomas more accurately.

4.4. Ratio of DTI-based parameters in LGG and HGG

The ratios of class numbers 14, 15 and 16 were significantly higher in HGGs than in LGGs. Class numbers 14, 15 and 16 seemed similar with regard to high DWI values. There was no significant difference between LGGs and HGGs in a past study (Kono et al., 2001), suggesting that grading tumours only by DWI is controversial. In our study, class numbers 3 and 5, which were not different between LGGs and HGGs, also had high DWI values. These results support the controversy regarding DWI and suggest that glioma grading only by DWI may be difficult.

Class numbers 14 and 15 had low FA values. In contrast, class number 16 had high FA values. Some researchers have reported that changes in FA in gliomas may indicate tumour cell infiltration (Schluter et al., 2005; Kallenberg et al., 2013). A reduction in FA seemed to be the common denominator among structural abnormalities (Wieshmann et al., 1999). Lower FA values were seen in LGGs in one study (Inoue et al., 2005), whereas another study showed no significant differences between LGGs and HGGs (Goebell et al., 2006). In our study, both increases and decreases in FA were seen in tumours. Particularly, class numbers 13 and 16 showed that high FA values were also included in HGGs.

Class numbers 14–16, which had significantly higher values in HGGs, seemed to have low MD values. However, most classes (numbers 2, 3, 5, 7, 8, 9, 10, 11, 12 and 13) with low MD values were not different between HGGs and LGGs. These results suggest that it is difficult to predict glioma grade only by using one parameter, such as DWI, FA or MD as discussed in many previous studies.

4.5. Glioma grading

The current gold standard for determining glioma grade is histopathological assessment. However, the limitations of histopathological assessment because of the heterogeneity of gliomas are well known. First, there is a possibility of sampling error. Because only a few small pieces of tissue are assessed and we tend to examine T1-enhancing lesions, the most malignant tissue may not be obtained. Sampling errors may occur especially for biopsy only (Law et al., 2006). Even if we resect most tumours, a thorough investigation is not always made in the

resected tumour, and this is a histopathological limitation at present. Several studies have been conducted to evaluate more accurate selection of targets by using positron emission tomography (PET) images with ^{18}F-labelled fluorodeoxyglucose and ^{11}C-labelled methionine to reduce sampling errors (Levivier et al., 1995; Pirotte et al., 2004). However, the radiotracer injection in PET is invasive because of radiation exposure. By using DTcIs, we can non-invasively predict the grade of gliomas with accuracy and may perform regional grading of glioma, which is useful for targeting biopsy. Gliomas are heterogeneous tumours. If we can preoperatively predict the regional grading of a tumour, we can know which region must be resected, including peritumoural oedematous lesions. Second, some LGGs develop into HGGs, and ≥10% of gliomas dedifferentiate into more malignant grades (Law et al., 2006). We cannot know when tumour grade progresses. By using regional grading based on DTcIs, we can clarify when LGGs progress into HGGs during follow-up and provide an appropriate adjuvant treatment at the optimum time. The potential benefit of the proposed method in the present study could be emphasized by undertaking a prospective, randomized controlled study.

5. Conclusion

This study applied a two-level clustering approach, which consisted of SOM followed by the KM++ algorithm, for unsupervised clustering of a large number of input vectors with multiple features by DTI. The greatest point of the method is to enable obtaining novel clustering images called DTcIs, that can give visual grading of glioma and be helpful in differentiating between LGGs and HGGs without pathological information. Our new approach could lead to more accurate non-invasive grading and more appropriate treatment.

Acknowledgements

References

Alhoniemi, E., Hollmen, J., Simula, O., Vesanto, J., 1999. Process monitoring and modeling using the self-organizing map. Integrated Computer-Aided Engineering 6, 3–14.
Arthur, D., Vassilvitskii, S., 2007. k-means++: the advantages of careful seeding. Proceedings of the Eighteenth Annual ACM-SIAM Symposium on Discrete AlgorithmsSociety for Industrial and Applied Mathematics, Philadelphia, PA, USA.
Beccali, M., Cellura, M., Lo Brano, V., Marvuglia, A., 2004. Forecasting daily urban electric load profiles using artificial neural networks. Energy Conversion and Management 45, 2879–2900.
Boretius, S., Escher, A., Dallenga, T., Wrzos, C., Tammer, R., Brück, W., et al., 2012. Assessment of lesion pathology in a new animal model of MS by multiparametric MRI and DTI. Neuroimage 59, 2678–2688. http://dx.doi.org/10.1016/j.neuroimage.2011.08.05121914485.
Brugger, D., Bogdan, M., Rosenstiel, W., 2008. Automatic cluster detection in Kohonen's SOM. IEEE Transactions on Neural Networks / a Publication of the IEEE Neural Networks Council, 19 442–459 http://dx.doi.org/10.1109/TNN.2007.90955618334364.
Camelo-Piragua, S., Jansen, M., Ganguly, A., Kim, J.C., Cosper, A.K., Dias-Santagata, D., et al., 2011. A sensitive and specific diagnostic panel to distinguish diffuse astrocytoma from astrocytosis: chromosome 7 gain with mutant isocitrate dehydrogenase 1 and p53. Journal of Neuropathology and Experimental Neurology 70, 110–115. http://dx.doi.org/10.1097/NEN.0b013e31820565f921343879.

Chang, C.-C., Lin, C.-J., 2011. LIBSVM: A library for support vector machines. ACM Transactions on Intelligent Systems and Technology 2, 1–27.
Chavez-Alvarez, R., Chavoya, A., Mendez-Vazquez, A., 2014. Discovery of possible gene relationships through the application of self-organizing maps to DNA microarray databases. PloS One 9, e93233. http://dx.doi.org/10.1371/journal.pone.009323324699245.
Chuang, K.H., Chiu, M.J., Lin, C.C., Chen, J.H., 1999. Model-free functional MRI analysis using Kohonen clustering neural network and fuzzy C-means. IEEE Transactions on Medical Imaging 18, 1117–1128. http://dx.doi.org/10.1109/42.81932210695525.
Dosenbach, N.U., Nardos, B., Cohen, A.L., Fair, D.A., Power, J.D., Church, J.A., et al., 2010. Prediction of individual brain maturity using fMRI. Science (New York, N.Y.) 329, 1358–1361. http://dx.doi.org/10.1126/science.119414420829489.
Ehsani, A.H., Quiel, F., 2008. Application of self organizing map and SRTM data to characterize yardangs in the Lut desert, Iran. Remote Sensing of Environment 112, 3284–3294.
Filippi, C.G., Ulug, A.M., Ryan, E., Ferrando, S.J., van Gorp, W., 2001. Diffusion tensor imaging of patients with HIV and normal-appearing white matter on MR images of the brain. AJNR. American Journal of Neuroradiology 22, 277–28311156769.
Goebell, E., Paustenbach, S., Vaeterlein, O., Ding, X.Q., Heese, O., Fiehler, J., et al., 2006. Low-grade and anaplastic gliomas: differences in architecture evaluated with diffusion-tensor MR imaging. Radiology 239, 217–222. http://dx.doi.org/10.1148/radiol.238305005916484348.
Griffith, J.L., Shimony, J.S., Cousins, S.A., Rees, S.E., McCurnin, D.C., Inder, T.E., et al., 2012. MR imaging correlates of white-matter pathology in a preterm baboon model. Pediatric Research 71, 185–191. http://dx.doi.org/10.1038/pr.2011.3322258130.
Holodny, A.I., Ollenschleger, M.D., Liu, W.C., Schulder, M., Kalnin, A.J., 2001. Identification of the corticospinal tracts achieved using blood-oxygen-level-dependent and diffusion functional MR imaging in patients with brain tumors. AJNR. American Journal of Neuroradiology 22, 83–8811158892.
Hothorn, T., Hornik, K., van de Wiel, M., Zeileis, A., 2006. A lego system for conditional inference. American Statistician 60, 257–263.
Hsu, C.-W., Chang, C.-C., Lin, C.-J., 2003. A Practical Guide to Support Vector ClassificationDepartment of Computer Science, National Taiwan University.
Inoue, T., Ogasawara, K., Beppu, T., Ogawa, A., Kabasawa, H., 2005. Diffusion tensor imaging for preoperative evaluation of tumor grade in gliomas. Clinical Neurology and Neurosurgery 107, 174–180. http://dx.doi.org/10.1016/j.clineuro.2004.06.01115823671.
Ironside, J.W., 1994. Update on central nervous system cytopathology. II. Brain smear technique. Journal of Clinical Pathology 47, 683–6887962615.
Jenkinson, M., Beckmann, C.F., Behrens, T.E., Woolrich, M.W., Smith, S.M., 2012. FSL. Neuroimage 62, 782–790. http://dx.doi.org/10.1016/j.neuroimage.2011.09.01521979382.
Jezzard, P., Balaban, R.S., 1995. Correction for geometric distortion in echo planar images from B0 field variations. Magnetic Resonance in Medicine: Official Journal of the Society of Magnetic Resonance in Medicine / Society of Magnetic Resonance in Medicine 34, 65–737674900.
Jezzard, P., Clare, S., 1999. Sources of distortion in functional MRI data. Human Brain Mapping 8, 80–8510524596.
Jin, H., Shum, W.H., Leung, K.S., Wong, M.L., 2004. Expanding self-organizing map for data visualization and cluster analysis. Information Sciences 163, 157–173.
Jones, D.K., Horsfield, M.A., Simmons, [!(%xInRef|ce:surname)!], A., 1999. Optimal strategies for measuring diffusion in anisotropic systems by magnetic resonance imaging. Magnetic Resonance in Medicine: Official Journal of the Society of Magnetic Resonance in Medicine / Society of Magnetic Resonance in Medicine 42 (3), 515–52510467296.
Kallenberg, K., Goldmann, T., Menke, J., Strik, H., Bock, H.C., Stockhammer, F., et al., 2013. Glioma infiltration of the corpus callosum: early signs detected by DTI. Journal of Neuro-Oncology 112, 217–222. http://dx.doi.org/10.1007/s11060-013-1049-y23344787.
Kao, H.W., Chiang, S.W., Chung, H.W., Tsai, F.Y., Chen, C.Y., 2013. Advanced MR imaging of gliomas: an update. BioMed Research International 2013, 1–14. http://dx.doi.org/10.1155/2013/97058623862163.
Klawiter, E.C., Schmidt, R.E., Trinkaus, K., Liang, H.F., Budde, M.D., Naismith, R.T., et al., 2011. Radial diffusivity predicts demyelination in ex vivo multiple sclerosis spinal cords. Neuroimage 55, 1454–1460. http://dx.doi.org/10.1016/j.neuroimage.2011.01.00721238597.
Klingberg, T., Vaidya, C.J., Gabrieli, J.D., Moseley, M.E., Hedehus, M., 1999. Myelination and organization of the frontal white matter in children: a diffusion tensor MRI study. Neuroreport 10, 2817–282110511446.
Kohonen, T., 1995. Self-Organizing MapsSpringer, Berlin.
Kono, K., Inoue, Y., Nakayama, K., Shakudo, M., Morino, M., Ohata, K., et al., 2001. The role of diffusion-weighted imaging in patients with brain tumors. AJNR. American Journal of Neuroradiology 22, 1081–108811415902.
Lam, W.W., Poon, W.S., Metreweli, C., 2002. Diffusion MR imaging in glioma: does it have any role in the pre-operation determination of grading of glioma? Clinical Radiology 57, 219–225. http://dx.doi.org/10.1053/crad.2001.074111952318.
Law, M., Oh, S., Babb, J.S., Wang, E., Inglese, M., Zagzag, D., et al., 2006. Low-grade gliomas: dynamic susceptibility-weighted contrast-enhanced perfusion MR imaging – prediction of patient clinical response. Radiology 238, 658–667. http://dx.doi.org/10.1148/radiol.23820421801639688.
Levivier, M., Goldman, S., Pirotte, B., Brucher, J.M., Balériaux, D., Luxen, A., et al., 1995. Diagnostic yield of stereotactic brain biopsy guided by positron emission tomography with [^{18}F]fluorodeoxyglucose. Journal of Neurosurgery 82, 445–452. http://dx.doi.org/10.3171/jns.1995.82.3.04457861223.
Liao, W., Chen, H., Yang, Q., Lei, X., 2008. Analysis of fMRI data using improved self-organizing mapping and spatio-temporal metric hierarchical clustering. IEEE Transactions on Medical Imaging 27, 1472–1483. http://dx.doi.org/10.1109/TMI.2008.92398718815099.

Louis, D.N., Ohgaki, H., Wiestler, O.D., Cavenee, W.K., 2007a. WHO Classification of Tumours of the Central Nervous systemfourth edition. WHO, Lyon, http://dx.doi.org/10.1007/s00401-007-0243-417618441.

Louis, D.N., Ohgaki, H., Wiestler, O.D., Cavenee, W.K., Burger, P.C., Jouvet, A., et al., 2007b. The 2007 WHO classification of tumours of the central nervous system. Acta Neuropathologica 114, 97–109. http://dx.doi.org/10.1007/s00401-007-0243-417618441.

Lu, H.C., Hsieh, J.C., Chang, T.S., 2006. Prediction of maximum daily ozone level using combined neural network and statistical characteristics. Atmospheric Research 81, 124–139.

MacQueen, J.B., 1967. Some methods for classification and analysis of multivariate observations. Proceedings of the Fifth Symposium on Math, Statistics, and Probability, BerkeleyUniversity of California Press, CA.

Mangin, J.F., Poupon, C., Clark, C., Le Bihan, D., Bloch, I., 2002. Distortion correction and robust tensor estimation for MR diffusion imaging. Medical Image Analysis 6, 191–19812270226.

McLendon, R.E., Halperin, E.C., 2003. Is the long-term survival of patients with intracranial glioblastoma multiforme overstated? Cancer 98, 1745–1748. http://dx.doi.org/10.1002/cncr.1166614534892.

Ohgaki, H., Kleihues, P., 2007. Genetic pathways to primary and secondary glioblastoma. American Journal of Pathology 170, 1445–1453. http://dx.doi.org/10.2353/ajpath.2007.07001117456751.

Ota, K., Oishi, N., Ito, K., Fukuyama, H., 2014. A comparison of three brain atlases for MCI prediction. Journal of Neuroscience Methods 221, 139–15024140118.

Peltier, S.J., Polk, T.A., Noll, D.C., 2003. Detecting low-frequency functional connectivity in fMRI using a self-organizing map (SOM) algorithm. Human Brain Mapping 20, 220–226. http://dx.doi.org/10.1002/hbm.1014414673805.

Pirotte, B., Goldman, S., Massager, N., David, P., Wikler, D., Lipszyc, M., et al., 2004. Combined use of 18F-fluorodeoxyglucose and 11C-methionine in 45 positron emission tomography-guided stereotactic brain biopsies. Journal of Neurosurgery 101, 476–483. http://dx.doi.org/10.3171/jns.2004.101.3.047615352606.

Price, S.J., Burnet, N.G., Donovan, T., Green, H.A., Peña, A., Antoun, N.M., et al., 2003. Diffusion tensor imaging of brain tumours at 3T: a potential tool for assessing white matter tract invasion? Clinical Radiology 58, 455–46212788314.

Rajini, H.N., Bhavani, R., 2012. Automatic MR brain tumor detection using possibilistic C-means and K-means clustering with color segmentation. International Journal of Computer Applications 56, 11–17.

Robin, X., Turck, N., Hainard, A., Tiberti, N., Lisacek, F., Sanchez, J.C., et al., 2011. pROC: an open-source package for R and S+ to analyse and compare ROC curves. BMC Bioinformatics 12, 77. http://dx.doi.org/10.1186/1471-2105-12-7721414208.

Rousseeuw, P.J., 1987. Silhouettes: a graphical aid to the interpretation and validation of cluster analysis. Journal of Computational and Applied Mathematics 20, 53–65.

Sanai, N., Berger, M.S., 2008. Glioma extent of resection and its impact on patient outcome. Neurosurgery 62, 753–76418496181.

Scherer, H.J., 1938. Structural development in gliomas. American Journal of Cancer 34, 333–351.

Schlüter, M., Stieltjes, B., Hahn, H.K., Rexilius, J., Konrad-verse, O., Peitgen, H.O., 2005. Detection of tumour infiltration in axonal fibre bundles using diffusion tensor imaging. International Journal of Medical Robotics + Computer Assisted Surgery: MRCAS 1, 80–86. http://dx.doi.org/10.1002/rcs.3117518394.

Scott, J.N., Brasher, P.M., Sevick, R.J., Rewcastle, N.B., Forsyth, P.A., 2002. How often are nonenhancing supratentorial gliomas malignant? A population study. Neurology 59, 947–94912297589.

Smith, S.M., Jenkinson, M., Woolrich, M.W., Beckmann, C.F., Behrens, T.E., Johansen-Berg, H., et al., 2004. Advances in functional and structural MR image analysis and implementation as FSL. NeuroImage 23 (Suppl. 1), S208–S219. http://dx.doi.org/10.1016/j.neuroimage.2004.07.05115501092.

Stadnik, T.W., Chaskis, C., Michotte, A., Shabana, W.M., van Rompaey, K., Luypaert, R., et al., 2001. Diffusion-weighted MR imaging of intracerebral masses: comparison with conventional MR imaging and histologic findings. AJNR. American Journal of Neuroradiology 22, 969–97611337344.

Thomassey, S., Happiette, M., 2007. A neural clustering and classification system for sales forecasting of new apparel items. Applied Soft Computing 7, 1177–1187.

Thomsen, H.S., 2003. Guidelines for contrast media from the European Society of Urogenital Radiology. AJR. American Journal of Roentgenology 181, 1463–1471. http://dx.doi.org/10.2214/ajr.181.6.181146314627556.

Tien, R.D., Felsberg, G.J., MacFall, J., Friedman, H., Brown, M., 1994. MR imaging of high-grade cerebral gliomas: value of diffusion-weighted echoplanar pulse sequences. AJR. American Journal of Roentgenology 162, 671–677. http://dx.doi.org/10.2214/ajr.162.3.81095208109520.

Vapnik, V.N., 1998. The Nature of Statistical Learning TheorySpringer Verlag, New York.

Velmurugan, T., Santhanam, T., 2010. Computational complexity between K-means and K-medoids clustering algorithms for normal and uniform distributions of data points. Journal of Computer Science 6, 363–368.

Vesanto, J., Alhoniemi, E., 2000. Clustering of the self-organizing map. IEEE Transactions on Neural Networks / a Publication of the IEEE Neural Networks Council, 11 586–600 http://dx.doi.org/10.1109/72.84673118249787.

Vijayakumar, C., Damayanti, G., 2007. Pant R, Sreedhar CM. Segmentation and grading of brain tumors on apparent diffusion coefficient images using self-organizing maps. Computerised Medical Imaging and Graphics 31, 473–48417572068.

Wang, J., Delabie, J., Aasheim, H.C., Smeland, E., Myklebost, O., 2002. Clustering of the SOM easily reveals distinct gene expression patterns: results of a reanalysis of lymphoma study. BMC Bioinformatics 3, 1–9.

Watanabe, M., Tanaka, R., Takeda, N., 1992. Magnetic resonance imaging and histopathology of cerebral gliomas. Neuroradiology 34, 463–4691436452.

Wieshmann, U.C., Clark, C.A., Symms, M.R., Franconi, F., Barker, G.J., Shorvon, S.D., 1999. Reduced anisotropy of water diffusion in structural cerebral abnormalities demonstrated with diffusion tensor imaging. Magnetic Resonance Imaging 17, 1269–127410576712.

Zacharaki, E.I., Wang, S., Chawla, S., Soo Yoo, D., Wolf, R., Melhem, E.R., et al., 2009. Classification of brain tumor type and grade using MRI texture and shape in a machine learning scheme. Magnetic Resonance in Medicine: Official Journal of the Society of Magnetic Resonance in Medicine / Society of Magnetic Resonance in Medicine 62, 1609–1618. http://dx.doi.org/10.1002/mrm.2214719859947.

Treatment for Infection of Artificial Dura Mater Using Free Fascia Lata

Takashi Nakano, MD,* Katsuhiro Yoshikawa, MD, PhD,* Takeharu Kunieda, MD, PhD,†
Yoshiki Arakawa, MD, PhD,† Takayuki Kikuchi, MD, PhD,† Satoko Yamawaki, MD, PhD,*
Motoko Naitoh, MD, PhD,* Katsuya Kawai, MD, PhD,* and Shigehiko Suzuki, MD, PhD*

Abstract: Synthetic artificial dura mater materials, such as expanded polytetrafluoroethylene sheets, are widely used in dura mater reconstruction in cases involving brain tumors or trauma surgery. In patients with postoperative infection related to the use of artificial dura mater, surgical debridement of the infected wound and removal of the artificial dura mater materials are necessary to control infection. In cases involving cerebrospinal fluid leakage, dura mater reconstruction must be performed immediately. Many useful techniques for performing dura mater reconstruction to treat postoperative infection have been reported; however, some have drawbacks with respect to the need for microvascular anastomosis or difficulties in obtaining watertight closure.

We successfully treated 6 patients with postoperative artificial dura mater infection using free thigh fascia lata. Some surgeons believe that the use of free fascia in infected wounds is dangerous because free fascia is a non–vascularized tissue. However, performing complete debridement and covering such free fascia with well-vascularized tissue allow the fascia to become vascularized and tolerant of infection. Therefore, if the blood flow in the scalp is acceptable after a sufficient debridement, free fascia lata can be used for reconstruction in patients with postoperative infection of artificial dura mater. Furthermore, skull reconstruction can be performed safely and easily with solid-type artificial bone, sometimes combined with tissue expansion, thus resulting in good aesthetic outcomes.

Key Words: Dura infection, artificial dura mater, tissue expander, free fascia lata

(J Craniofac Surg 2014;25: 1252–1255)

What Is This Box?
A QR Code is a matrix barcode readable by QR scanners, mobile phones with cameras, and smartphones. **The QR Code links to the online version of the article.**

Synthetic artificial dura mater materials, such as expanded polytetrafluoroethylene (ePTFE) sheets, are often used in dura mater reconstruction in the field of neurosurgery. However, there are some reports of infection of artificial dura mater.[1] With respect to the treatment of infection, antibiotic therapy alone is inadequate, and sufficient debridement and removal of alien substances are required. In cases in which cerebrospinal fluid leakage is observed, the dura mater must be reconstructed with self-tissue, not an artificial substance, and watertight suturing is important to prevent hydrorrhea cerebrospinalis. For reconstruction, free flaps, such as anterolateral thigh flaps with fascia lata or rectus abdominis muscle and fascial flaps, and pedicle flaps, such as pericranial flaps or galeal flaps, are used. Free fascia without any blood flow is also used with muscle or pedicle flaps, which tend to have a rich blood flow.

In cases of postoperative infection of artificial dura mater material, we use free fascia lata to reconstruct the dura mater and cover it with a well-vascularized scalp. Using this technique, we achieved a successful suppression of infection. If necessary, we perform a second operation with solid-type artificial bone to obtain aesthetically satisfactory results.

PATIENTS AND METHODS

A retrospective analysis was performed among the patients who underwent reconstruction of the dura mater after infection of artificial dura mater material between May 2009 and August 2013. A total of 6 patients were included in this study.

Free fascia lata was used to cover the dura mater defects in a watertight fashion. The amount of free fascia lata used in each case was determined according to the defect size. After reconstruction of the dura mater with free fascia lata, the free fascia lata was covered with scalp tissue, which has a rich blood flow.

RESULTS

All 6 patients were treated with free fascia lata. The ages of the patients ranged from 28 to 63 years, with a mean age of 43 years. The size of free fascia lata needed for reconstruction ranged from 7 × 5 to 13 × 15 cm. In 5 cases, no capsule formation was observed under the artificial dura mater. In the remaining case, the formation of a capsule was found; however, the capsule was judged to be contaminated and excised so that reconstruction of the dura mater was required. No patients had diabetes. Subdural abscesses were observed in 3 cases, and epidural abscesses were observed in 3 cases. The primary diseases included arteriovenous malformation, meningioma, glioblastoma, and temporal lobe epilepsy. In 5 cases, pathogenic bacteria were identified in the artificial dura mater material, 3 cases of which involved methicillin-resistant *Staphylococcus aureus* (MRSA). In 1 case, no pathogenic bacteria were found in either the artificial dura mater material or swab specimens of the wound, although white blood cells were detected

TABLE 1. Six Patients Treated With a Free Fascia Lata for Infection of Artificial Dura Mater

Patient	Age	Sex	Diagnosis	Fascia Lata Size (cm)	Capsule Formation	Primary Disease	Phlogogenic Fungus	Period From Primary Operation	Skull Reconstruction	Period Between First and Second Operation
1	28	Female	Subdural abscess	15 × 12	+	Arteriovenous malformation	MRSA	2 mo	+	8 mo
2	38	Female	Epidural abscess	10 × 12	−	Temporal lobe epilepsy	MRSA	8 mo	+	9 mo (6-mo expander)
3	43	Female	Subdural abscess	12 × 9	−	Convexity meningioma	Uncertain	2 mo	+	6 mo
4	63	Male	Epidural abscess	6 × 10	−	Glioblastoma	E. faecalis	1 wk	+	4 mo
5	37	Male	Subdural abscess	13 × 15	−	Intraventricular meningioma	MRCNS	2 mo	+	2 mo
6	48	Male	Epidural abscess	7 × 5	−	Hemangioblastoma	MRSA	2 wk	−	−

E. faecalis, Enterococcus faecalis; MRCNS, methicillin-resistant coagulase-negative Staphylococcus.

in these samples. In all cases, antibiotic therapy was administered continuously before the surgery (Table 1).

After debridement and reconstruction of the dura mater with the free fascia lata, we achieved suppression of infection without complications in all patients. Skull reconstruction was performed in 5 cases, 1 case of which involved the use of a tissue expander. The average period from fascia lata grafting to skull reconstruction was 5.8 months (2–9 mo).

CLINICAL REPORTS

Patient 2

A 38-year-old woman had intractable temporal lobe epilepsy. Focal resection was performed, and the dura mater was repaired with an ePTFE sheet. The patient exhibited fluid collection under her scalp after the surgery, which did not heal despite the administration of antibiotics for 2 months. Debridement was performed, and the bone graft was removed. The patient had no symptoms of infection and returned for a follow-up visit; however, 6 months later, a cutaneous fistula developed on the scar. She was therefore referred to the plastic surgery department for treatment of an ongoing intractable infection.

Computed tomographic (CT) scan showed a low-density area between the scalp and the artificial dura mater material (Fig. 1A) with extensive cranial bone loss (Fig. 1B). The diagnosis was an epidural abscess, and infection of the artificial dura mater material was strongly suspected. We therefore planned a 2-staged operation.

During the first procedure, a skin incision was created along the site of the previous incision, sufficient debridement of the infected area was performed, and the artificial dura mater material was removed. The dura mater was reconstructed using a free fascia lata measuring 10 × 12 cm in size harvested from the patient's left thigh (Figs. 1C, D). The dural defect was closed with the graft in a watertight fashion (Fig. 1E). The skin fistula was resected, and the damaged portion of the skin was debrided. The scalp was directly closed without excessive tension. Methicillin-resistant S. aureus was detected in a bacteriological culture of the artificial dura mater material. No recurrence of infection or cerebrospinal fluid leakage was observed postoperatively (Fig. 1F).

Six months later, cranioplasty was planned. In this case, because there was an insufficient amount of scalp tissue to cover the artificial bone graft, scalp stretching using a tissue expander was performed before cranioplasty (Figs. 2 A, B). Cranioplasty with solid-type artificial bone was performed, which resulted in an
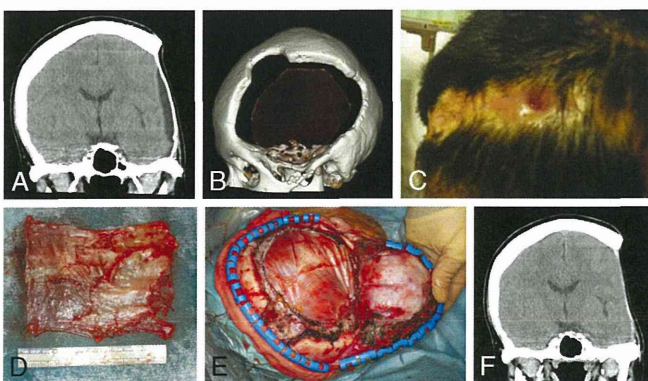

FIGURE 1. A, Preoperative CT scan shows a low-density area between the scalp and artificial dura mater. B, Three-dimensional CT scan demonstrates extensive cranial bone loss. C, A cutaneous fistula appeared on the scar. D, A free fascia lata graft measuring 10 × 12 cm in size harvested from the patient's left thigh. E, The dural defect was closed using the fascia lata in a watertight fashion. F, Postoperative CT scan shows the reconstructed dura mater with the fascia lata in addition to the disappearance of the low-density area.
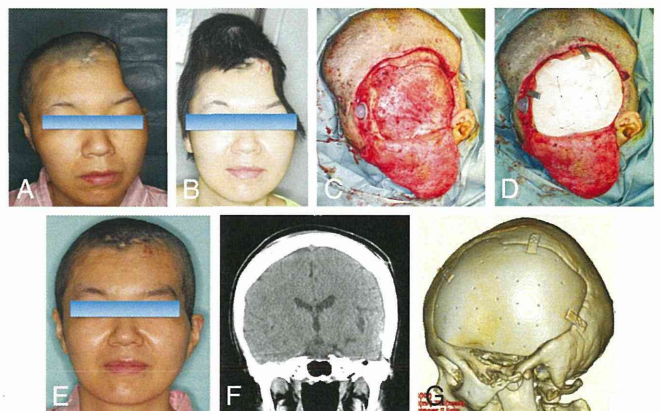
FIGURE 2. A, A noticeable contour deformity in the skull before cranioplasty. B, Scalp stretching with a tissue expander was performed before cranioplasty. C, After detaching the scalp from the fascia completely, a continuous oozing from the fascia lata was observed. D, Cranioplasty with solid-type artificial bone was performed. E, An aesthetically satisfactory result was obtained after cranioplasty. F, Postoperative CT scan shows symmetry of shape with no low-density areas. G, Postoperative three-dimensional CT scan of the skull and the solid-type artificial bone.

© 2014 Mutaz B. Habal, MD

1253

aesthetically successful outcome (Figs. 2C–G). It is notable that a continuous oozing from the surface of the fascia lata persisted, even after the scalp was completely detached from the fascia (Fig. 2C). Careful hemostasis was achieved with bipolar coagulation to prevent epidural hematoma formation.

Patient 5

A 37-year-old man presented with a ventricular meningioma (Fig. 3A). Endoscopic gross total resection was performed (Fig. 3B). One week after the surgery, he developed a fever of unknown origin with a white blood cell count over 10,000/cu mm, and empiric antibiotic therapy was started. Despite the administration of antibiotics, the patient's consciousness level deteriorated, and CT scan showed a large low-density area between the left basal ganglion region and deep white matter (Fig. 3C). This suggested that the hydrocephalus was caused by an impaired venous return, and the patient underwent external decompression with an ePTFE sheet. After the operation, his consciousness level and symptoms improved. Nevertheless, 1 week later, he developed fluid collection under the scalp, and methicillin-resistant coagulase-negative *Staphylococcus* was detected in a bacteriological culture of wound swab specimens. Wound irrigation was repeated; however, the effusion did not decrease, and the patient was therefore referred to the plastic surgery department for treatment of an intractable infection.

Computed tomographic scan showed a low-density area around the artificial dura mater material with extensive cranial bone loss (Fig. 3D). We therefore planned a 2-staged operation to treat the infection.

In the first procedure, sufficient debridement in the infected area was performed, and the artificial dura mater material was removed. The dura mater was reconstructed using a free fascia lata measuring 13 × 15 cm in size harvested from the patient's left thigh.
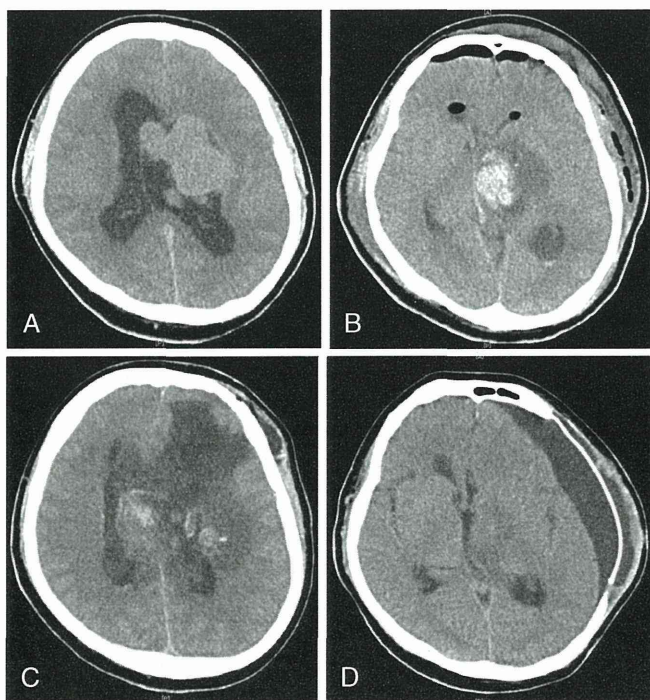

FIGURE 3. A, A ventricular meningioma was diagnosed. B, Endoscopic gross total resection was performed. C, A large low-density area was observed between the left basal ganglion region and the deep white matter after the gross total resection. D, A low-density area was noted around the artificial dura mater after external decompression.
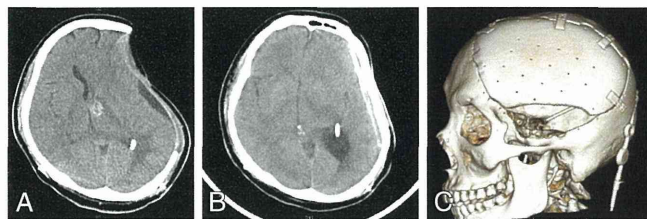

FIGURE 4. A, Computed tomographic scan performed 2 months after the first operation. B, Postoperative CT scan showed no low-density areas around the fascia lata or artificial bone. C, Postoperative three-dimensional CT scan of the skull and solid-type artificial bone.

The dural defect was closed with the graft in a watertight fashion, and the scalp was closed directly without excessive tension. External ventricular drainage was used to treat the obstructive hydrocephalus. No recurrence of infection was observed postoperatively (Fig. 4A).

Two months later, cranioplasty with solid-type artificial bone was performed, which resulted in a good outcome (Fig. 4B).

DISCUSSION

Synthetic artificial dura mater materials are widely used in neurosurgery; however, some cases of wound infection after dura mater reconstruction with synthetic artificial dura mater materials have been reported. The successful repair of infected artificial dura mater material depends on sufficient debridement, obtaining a watertight seal and using a well-vascularized tissue.[1,2] Some surgeons have reported on the treatment of postoperative infection of artificial dura mater materials using vascularized tissues. For example, Takagi et al[3] used a bipedicled pericranial flap and second-staged cranioplasty with the outer table of a calvarial bone graft in a patient with traumatic dural exposure. Shimada et al[4] reported reconstructing the dura mater using an anterolateral thigh flap with the fascia lata in a patient with a chronic abscess that developed after cranioplasty. Meanwhile, Soon Sung et al[5] and West et al[6] reported the use of the rectus abdominis muscle combined with a vascularized fascial perforator flap in patients undergoing skull base surgery. These authors used vascularized tissue to reconstruct the dura mater. On the other hand, Uemura et al[7] reported treating a case of artificial dura mater infection using a non–vascularized fascia lata combined with a rectus muscle free flap and staged cranioplasty. Although some surgeons have reported that capsule formation can make secondary reconstruction of the dura mater unnecessary,[8] others disagree.[9]

The fascia lata is the most commonly used autograft; it has been used for decades to yield predictable results.[10] A clear advantage of autografts is that the host response is rarely problematic. However, the use of autografts is limited because of morbidity associated with harvesting the tissue (eg, pain, bleeding, infection, hernia formation) as well as inconsistencies in the size, quantity, and quality of tissue.[11]

Autologous fascia grafts have previously been shown to become vascularized and resist infection compared with synthetic mesh in a rabbit model.[12] A free fascia lata graft has also been reported to be a reliable adjuvant to abdominal wall reconstruction in cases involving contaminated abdominal wounds in which the use of prosthetic materials is contraindicated and local tissue rearrangement is inadequate.[13] In addition, the fascia lata is tractable and can be sutured to the entire circumference of the dural defect in a watertight fashion; thus, the use of a free fascia lata covered with well-vascularized tissue reduces the rate of cerebrospinal leakage.[14] Scalp flaps allow for sufficient blood circulation and are resistant to infection, and it is easy to control the size of the epidural area.[2] Therefore, we treated the infected artificial dura mater material using a free

1254

© 2014 Mutaz B. Habal, MD

fascia lata with a well-vascularized scalp flap in all 6 patients, achieving successful control of infection in every case.

When performing artificial bone grafting during the second procedure, it is necessary to detach the adhesion between the scalp and the fascia lata, remove scar tissue to release contractures, and create space for the bone graft. Even after releasing the scalp flap from the fascia over the entire area, we observed a continuous oozing from the surface of the fascia lata that required coagulation hemostasis. On the basis of these findings, transplanted free fascia lata can be nourished through not only the scalp but also the surrounding dura mater before skull reconstruction, and the fascia remains vascularized even after skull reconstruction. Therefore, the artificial bone implant can be wrapped with vascularized tissue.[15] Furthermore, the free fascia lata is sufficiently tolerant of infection and useful for treating artificial dura mater infection. However, if the scalp defects are so large that the dura mater cannot be covered with a well-vascularized local scalp flap, free flaps must be used for reconstruction.

After the infection fully resolves, the second procedure can be performed. Before performing skull reconstruction, when the strain of the skin is strong, we use tissue expanders, which constitute a reliable method of providing an additional cutaneous and subcutaneous tissue, thereby optimizing contour and color matching. Tissue expansion is the most useful method for making up for the deficit of the scalp and allowing for complete hair coverage. The expanders, if used, are removed after expansion, and the reconstructive implant (solid-type artificial bone) is then placed. The postoperative skull contour was maintained satisfactorily in all of the present cases, and aesthetically good results were achieved in terms of contouring, minimum scaring, and hair coverage.

REFERENCES

1. Nakagawa S, Hayashi T, Anegawa S, et al. Postoperative infection after duraplasty with expanded polytetrafluoroethylene sheet. *Neurol Med Chir (Tokyo)* 2003;43:120–124
2. Chang DW, Langstein HN, Gupta A, et al. Reconstructive management of cranial base defects after tumor ablation. *Plast Reconstr Surg* 2001;107:1346–1355
3. Takagi M, Kiyokawa K, Sakamoto A, et al. Two-stage reconstructive surgery of a patient with head trauma resulting in extensive cranial bone and dura mater loss caused by postoperative infection: usefulness of a pericranial flap for dura mater reconstruction. *J Craniofac Surg* 2006;17:584–590
4. Shimada K, Ishikura N, Heshiki T, et al. Treatment for chronic abscess after cranioplasty: reconstruction of dura maters using the anterolateral thigh flap with fascia lata. *J Craniofac Surg* 2007;18:1305–1308
5. Soon Sung K, Hak C. Staged reconstruction of infected dura mater using vascularized rectus abdominis muscle. *J Craniofac Surg* 2012;23:1741–1743
6. West CA, Towns G, Bachelor AG, et al. Reconstruction of skull base and dura using rectus abdominis muscle combined with a vascularised fascial perforator flap. *J Plast Reconstr Aesthet Surg* 2006;59:631–635
7. Uemura T, Suse T, Yokoyama T, et al. Staged cranial reconstruction after epidural abscess associated with dural substitute exposure. *J Craniofac Surg* 2002;13:415–417
8. Nagasao T, Shinoda J, Horiguchi T, et al. Capsule formation can make secondary reconstruction of the dura mater unnecessary after cranial infection. *J Craniofac Surg* 2011;22:84–88
9. Fujioka M, Hayashida K, Murakamia C, et al. Preserving capsule formation after removal of dura mater complex increases risk of cranial infection relapse. *J Craniofac Surg* 2012;23:1579–1580
10. Albo ME, Richter HE, Brubaker L, et al. Burch colposuspension versus fascial sling to reduce urinary stress incontinence. *N Engl J Med* 2007;356:2143–2155
11. Walter AJ, Hentz JG, Magrina JF, et al. Harvesting autologous fascia lata for pelvic reconstructive surgery: techniques and morbidity. *Am J Obstet Gynecol* 2001;185:1354–1358
12. Disa JJ, Klein MH, Goldberg NH. Advantages of autologous fascia versus synthetic patch abdominal reconstruction in experimental animal defects. *Plast Reconstr Surg* 1996;97:801–806
13. Disa JJ, Goldberg NH, Carlton JM, et al. Restoring abdominal wall integrity in contaminated tissue-deficient wounds using autologous fascia grafts. *Plast Reconstr Surg* 1998;101:979–986
14. Abuzayed B, Kafadar AM, Oğuzoğlu ŞA, et al. Duraplasty using autologous fascia lata reenforced by on-site pedicled muscle flap: technical note. *J Craniofac Surg* 2009;20:435–438
15. Iguchi H, Motomura H. Simple maxillary reconstruction following total maxillectomy using artificial bone wrapped with vascularized tissue: five key points to ensure success. *Acta Otolaryngol* 2012;132:1–6

Intraoperative Dorsal Language Network Mapping by Using Single-Pulse Electrical Stimulation

Yukihiro Yamao,[1] Riki Matsumoto,[2]* Takeharu Kunieda,[1]* Yoshiki Arakawa,[1] Katsuya Kobayashi,[3] Kiyohide Usami,[3] Sumiya Shibata,[1] Takayuki Kikuchi,[1] Nobukatsu Sawamoto,[3] Nobuhiro Mikuni,[4] Akio Ikeda,[2] Hidenao Fukuyama,[5] and Susumu Miyamoto[1]

[1]Department of Neurosurgery, Kyoto University Graduate School of Medicine, Kyoto, Japan
[2]Department of Epilepsy, Movement Disorders and Physiology, Kyoto University Graduate School of Medicine, Kyoto, Japan
[3]Department of Neurology, Kyoto University Graduate School of Medicine, Kyoto, Japan
[4]Department of Neurosurgery, Sapporo Medical University School of Medicine, Sapporo, Japan
[5]Human Brain Research Center, Kyoto University Graduate School of Medicine, Kyoto, Japan

♦ ━━━ ♦
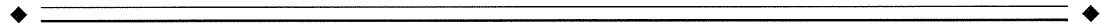
Abstract: The preservation of language function during brain surgery still poses a challenge. No intraoperative methods have been established to monitor the language network reliably. We aimed to establish intraoperative language network monitoring by means of cortico-cortical evoked potentials (CCEPs). Subjects were six patients with tumors located close to the arcuate fasciculus (AF) in the language-dominant left hemisphere. Under general anesthesia, the anterior perisylvian language area (AL) was first defined by the CCEP connectivity patterns between the ventrolateral frontal and temporoparietal area, and also by presurgical neuroimaging findings. We then monitored the integrity of the language network by stimulating AL and by recording CCEPs from the posterior perisylvian language area (PL) consecutively during both general anesthesia and awake condition. High-frequency electrical stimulation (ES) performed during awake craniotomy confirmed language function at AL in all six patients. Despite an amplitude decline (≤32%) in two patients, CCEP monitoring successfully prevented persistent language impairment. After tumor removal, single-pulse ES was applied to the white matter tract beneath the floor of the removal cavity in five patients, in order to trace its connections into the language cortices. In three patients in whom high-frequency ES of the white matter produced naming impairment, this "eloquent" subcortical site directly connected AL and PL, judging from the latencies and distributions of cortico- and subcortico-cortical evoked potentials. In conclusion, this study provided the direct evidence that AL, PL, and AF constitute the dorsal language network. Intraoperative CCEP monitoring is clinically useful for evaluating the integrity of the language network. *Hum Brain Mapp 35:4345–4361, 2014.* © 2014 Wiley Periodicals, Inc.

INTRODUCTION

The preservation of brain functions during surgery still poses a challenge in patients with brain tumors at or close to the eloquent areas. Motor evoked potentials (MEPs) have become one of the gold standard measures for monitoring the motor function in tumor and epilepsy surgery, since MEPs can indicate the integrity of the whole motor network: the motor cortices and the output pathway, the pyramidal tract [Macdonald, 2006]. The online, sequential recording of MEPs is of great clinical significance, since it can be performed under general anesthesia in patients with tumors at or close to the motor cortex or the pyramidal tract. On the contrary, no intraoperative methods have been established to monitor language function under general anesthesia. Therefore, intraoperative monitoring during awake craniotomy is often required to evaluate language function when the tumor is located at or around the language cortex or its white matter pathways.

Electrical stimulation (ES) during awake craniotomy has been developed by introducing a biphasic current-constant pulse and optimizing the intraoperative tasks [Berger et al., 1989; Whitaker and Ojemann, 1977]. After propofol was introduced in awake craniotomy in early 1990s, functional mapping with ES during awake craniotomy has become popular all over the world [July et al., 2009; Silbergeld et al., 1992]. High-frequency ES is commonly performed to identify the eloquent cortices such as the language area around tumors. In addition to the functional cortical mapping, the "eloquent" language fibers, namely the association fibers related to language function, have been extensively investigated with ES in pioneering work by Duffau [Duffau, 2008; Duffau et al., 2005]. However, these cortical- and subcortical ES methods could map only part of the language network, namely, the language cortex itself, or some (i.e., stimulus site) of the language fibers. As a result, even during awake craniotomy, no methods have yet been established to monitor the integrity of the language network during surgery, as opposed to MEPs for the motor network.

Recently, the development of diffusion tractography has enabled us to visualize the *in vivo* dissection of large white matter pathways in the living human brain. This noninvasive technique is widely applied for the preoperative evaluation of neurosurgery to trace major white matter pathways related to important brain functions, e.g., the pyramidal tract and the arcuate fasciculus (AF). It should be noted, however, that these white matter pathways are solely determined by the calculated anisotropic diffusion of water molecules, and thus the technique itself does not

probe their functional properties [Mori and van Zijl, 2002]. This limitation should be acknowledged, especially when the tracts representing the association fibers are traced into the cortices, since the terminations cannot be completely traced with this technique because of technical limitations such as the low signal-to-noise ratio at and around the cortices and fiber-crossings. Probabilistic diffusion tractography has been developed to overcome these limitations [Behrens et al., 2007], but it would be prudent to obtain complementary supporting evidence for clinical application to neurosurgery.

We have recently developed the *in vivo* electrical tract-tracing method using cortico-cortical evoked potentials (CCEPs) [Matsumoto et al., 2004]. In an extraoperative setting for presurgical evaluation of epilepsy surgery, single-pulse ES was applied directly to the cortex, and CCEPs were recorded from the remote cortex through cortico-cortical connections. In contrast to high-frequency (50 Hz) ES that aimed to define brain functions such as language, this invasive tract-tracing method with single-pulse ES provides us with a unique opportunity to track functional connectivity among different cortices electrophysiologically. This method has successfully delineated the language, motor, and parietofrontal networks [Enatsu et al., 2013; Matsumoto et al., 2004, 2007, 2012]. CCEP studies are relatively easy to perform: for each averaged result from a given stimulus site, it takes only 1–2 min with little patient cooperation; the chance of provoking seizures is extremely low, and the reproducibility or reliability of the data is very high [Matsumoto et al., 2007]. Therefore, the CCEP technique could be applicable in an intraoperative setting to identify and monitor the functionally important networks at or in the vicinity of lesions such as tumors.

The objective of the present study was to apply this single-pulse ES technique and to establish it as a novel intraoperative method to monitor the language network. Similarly to the intraoperative MEP recording, we aimed to monitor the degree of integrity of the language network by stimulating Broca's area and by recording CCEPs from Wernicke's area sequentially during the resection of the tumor located around the AF. In addition, during awake craniotomy, we attempted to obtain data supporting that the connections we traced by CCEPs and diffusion tractography were indeed involved in language function; 50 Hz ES was applied to the cortex and the white matter tracts to define their function, and 1 Hz ES was applied to the deeply seated tract in order to trace its cortical terminations at the language cortices by recording the cortical evoked responses [subcortico-cortical evoked potentials (SCEPs)].

311

TABLE I. Patient demographics

	Age	Gender	Tumor location	Language dominancy	Preoperative symptoms	Tumor pathology	WAB aphasia quotient Before surgery	After surgery 2–6 weeks	After surgery 3 months
Patient 1	28	Male	Ins, STG	Left	seizure, right hemiparesis	anaplastic astrocytoma	99.9	99.6	n.a.
Patient 2	31	Female	Ins, STG, MTG	Left	cognitive impairment, quadrantanopsia	WHO grade II–III astrocytoma	nl[a]	95.6	n.a.
Patient 3	19	Female	AG, SMG, PoCG	Left	seizure	DNT	100	100	n.a.
Patient 4	44	Female	AG, SMG, PoCG	Left	seizure	diffuse astrocytoma	99.5	80	100
Patient 5	38	Male	IFG	Left	seizure	oligodendroglioma	97.7	68.3	93
Patient 6	36	Female	SMG	Left	asymptomatic	DNT	100	100	n.a.

Ins = insula; MTG = middle temporal gyrus; PoCG = postcentral gyrus; SMG = supramarginal gyrus; AG = angular gyrus; STG = superior temporal gyrus; IFG = inferior frontal gyrus; DNT = dysembryoplastic neuroepithelial tumor; n.a. = not available.
[a]Normal language function by clinical examination.

MATERIALS AND METHODS

Subjects

Subjects were six patients (mean age 33 years, ranging from 19 to 44; 2 males) with brain tumors located close to the perisylvian language areas in the language-dominant left hemisphere. Language dominance was defined by the Wada test, which was performed using intra-carotid infusion of propofol [Takayama et al., 2004]. On neurological examination, four patients were unremarkable, one showed mild hemiparesis, and the other was found to have mild cognitive impairment and right upper quadrantanopsia. None of the patients showed any language impairment preoperatively, which was evaluated by the Japanese version of the Western Aphasia Battery (WAB) in five patients and formal neurological examination in one patient. Four patients had a history of partial seizures. The pathology of the tumor was a dysembryoplastic neuroepithelial tumor in two patients and glioma in four (diffuse astrocytoma, anaplastic astrocytoma, oligodendroglioma, and WHO Grade II–III astrocytoma; Table I).

Language function was evaluated with the WAB before and after surgery. Postoperative evaluation was performed within 6 weeks of surgery. For those who showed language impairment in the postoperative evaluation, a follow-up evaluation was performed 2 or 3 months after surgery.

Informed consent was obtained from all patients, and the present study was approved by the Kyoto University Graduate School and Faculty of Medicine, Ethics Committee (IRB C573).

In all patients, awake craniotomy was performed. A wide craniotomy exposing the distal end of the Sylvian fissure, the frontal operculum, and the posterior part of the superior and middle temporal gyri (STG and MTG) was

performed under general anesthesia using propofol. After the patients awoke, ES was performed mainly under local anesthesia.

Experimental Paradigm for Language Mapping and Preservation

Since the clinical goal was to preserve language function during surgical procedures, we attempted to map the dorsal pathway of the language network [Hickok and Poeppel, 2004]. By using 50 Hz and single-pulse ES for functional cortical/subcortical mapping and electrical tract-tracing, respectively, we aimed to map and monitor the dorsal language pathway in individual patients in the following order:

1. Before surgery, we localized the language cortex and the underlying white matter pathway (AF) by using functional magnetic resonance imaging (fMRI) and probabilistic diffusion tractography.
2. Under general anesthesia, we applied single-pulse ES to cortical regions around the anterior perisylvian language area (AL) that was localized based on anatomic criteria or by using fMRI before surgery. Based on the CCEP distribution in the lateral temporoparietal area, i.e., the CCEP connectivity pattern between the AL and the posterior perisylvian language areas (PLs), we determined the stimulus site (i.e., the putative AL) most appropriate for online CCEP monitoring. The integrity of the dorsal language pathway was then evaluated by online sequential CCEP monitoring during surgical procedures.
3. After the patient woke up, language assessment with batteries and CCEP recording was sequentially performed during surgical procedures. High-frequency

(50 Hz) ES was applied to the frontal stimulus site (the putative AL) to confirm its language function.

4. After tumor resection, we applied 50 Hz ES to the floor of the removal cavity to evaluate the function of the underlying white matter tract. We also applied single-pulse ES to the removal floor and recorded SCEPs from the ventorolateral frontal area and the lateral temporoparietal area. This white matter stimulation was performed in an attempt to trace the language-related tracts into the cortex so that we could evaluate the whole dorsal language pathway.

We describe the actual procedures of the aforementioned methods in the following paragraphs. Intraoperative methods are described first, followed by the preoperative noninvasive methods.

Intraoperative CCEP Mapping During General Anesthesia

After craniotomy under general anesthesia, strip or grid-type subdural electrodes were placed on the ventrolateral frontal and lateral temporoparietal cortices (see Fig. 1 for electrode configurations). The area of electrode placement was determined according to the noninvasive presurgical fMRI and tractography findings. The electrodes were made of platinum with a recording diameter of 3 mm and an inter-electrode distance of 1 cm (Unique Medical Co., Ltd., Tokyo, Japan).

The details of CCEP recording have been reported elsewhere [Matsumoto et al., 2004, 2007, 2012]. A 32-channel intraoperative monitoring system (MEE 1232 Neuromaster, equipped with MS 120B electrical stimulator; Nihon-Kohden, Tokyo, Japan) was used for delivering electric currents and for recording CCEPs and raw electrocorticogram (ECoG). All the data were digitized at a sampling rate of 5,000 Hz. To electrically trace the cortico-cortical connections *in vivo*, single-pulse ES was applied to the cortex in a bipolar fashion through a pair of adjacently placed electrodes. Square-wave electrical pulses of alternating polarity with a pulse width of 0.3 ms were delivered at a fixed frequency of 1 Hz and intensity of 10–15 mA. Recordings from subdural electrodes were referenced to a scalp electrode placed on the skin over the mastoid process contralateral to the side of electrode implantation. CCEPs were online obtained by averaging ECoGs time-locked to the stimulus onset, with a time window of 400 ms (Patients 1, 2, 4, 5, and 6) or 1,000 ms (Patient 3), and a band-pass filter of 0.5–1,500 Hz (Patients 4–6) or 1–1,500 Hz (Patients 1–3). The baseline was set at 4.8 ms (Patients 1, 2, 4, 5, and 6) or 12 ms (Patient 3) before stimulus onset. Two to three trials of 30 responses each were averaged separately to confirm the reproducibility of the responses. During recording, the patients were requested not to perform any tasks, including language tasks, while the patients fully awoke. Raw ECoG was simultaneously recorded to monitor afterdischarges and possible ECoG seizures and to record raw ECoG data for offline analysis.

The candidates for the frontal stimulus site were determined by checking the anatomy carefully [the pars opercularis (IFGop), the pars triangularis (IFGtr) and adjacent areas], the activation area in the fMRI language task, and the cortical terminations of the AF tract drawn by probabilistic diffusion tractography, all of which were implemented in a neuro-navigation system (Vector Vision Compact, BRAINLAB, Heimstetten, Germany). Three to eight pairs per patient were selected as the candidate stimulus sites. Single-pulse ES was delivered to each candidate site and CCEPs were recorded from the electrodes on the lateral temporoparietal area covering the putative PL. A large CCEP response with an N1 peak at 20–40 ms in the lateral temporoparietal area was considered to represent the cortico-cortical connections between the AL and PL [Matsumoto et al., 2004]. Based on the CCEP distribution, namely, the localization of the maximum CCEP response in the lateral temporoparietal area, the frontal stimulus site was selected for online sequential CCEP recordings. In other words, we determined the putative AL based on the locus of that led to peak CCEP amplitude evoked in PL (i.e., optimal CCEP connectivity pattern).

During the surgical procedure, under general anesthesia, the integrity of the dorsal language pathway was monitored online by stimulating the putative AL and by recording CCEP from the temporoparietal area, i.e., at and around the putative PL, in a sequential fashion at 10–15 min of intervals.

Intraoperative CCEP Mapping During Awake Craniotomy

After the patients woke up, during the surgical procedure, language function was evaluated during tumor removal by (1) 1 Hz stimulation to monitor the language network online, i.e., sequential CCEP recording and (2) examining the patient with language batteries: spontaneous speech, reading, picture naming, and word repetition.

In order to confirm language function at the frontal stimulus site, namely, the putative AL, language mapping was performed by conventional 50 Hz cortical ES (square-wave pulse of alternating polarity with a pulse width of 0.3 ms, 3–5 s, 5–12 mA). Reading and picture naming tasks were used. We judged the behaviors as significantly impaired when the findings were reproducible in the absence of afterdischarges [Matsumoto et al., 2011].

Intraoperative SCEP Mapping During Awake Craniotomy

In five out of six patients, after the removal of the tumor, we further evaluated the function and connectivity of the white matter pathway beneath the floor of the removal cavity. In Patient 2, subcortical stimulation was not feasible because of intraoperative brain edema. Strip or grid-type electrodes [1 × 4 strip (Patients 1, 3, 4, and 6), 2
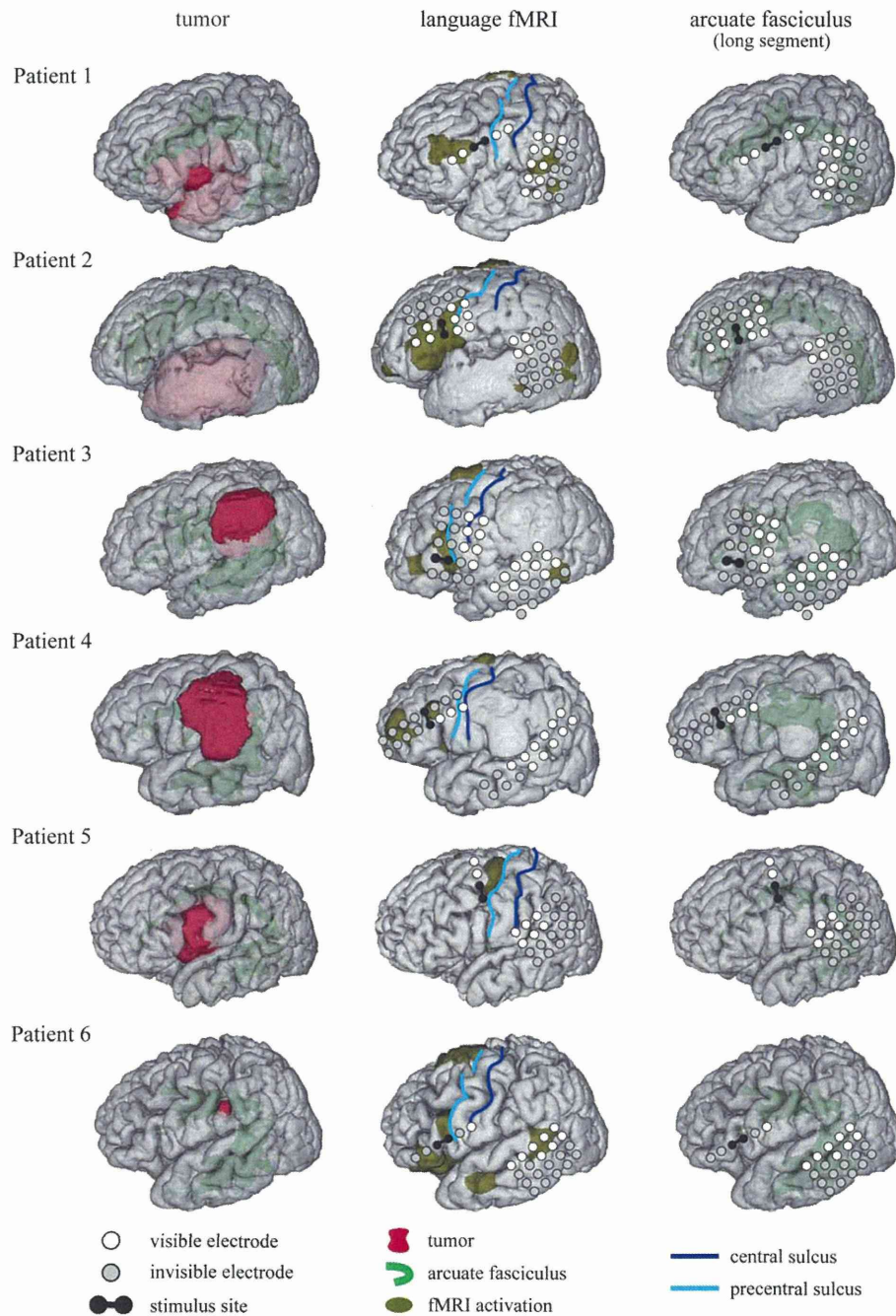
Figure 1.

Noninvasive anatomo-functional mapping of the dorsal language network. The left column: 3D MRI shows the long segment of the AF (green) and the tumor (red) around the AF. The middle column: The anterior and posterior perisylvian language cortices defined by *shiritori* word generation fMRI (dark yellow) are shown in comparison with the subdural electrodes. Only the activation areas outside the pre- and postcentral gyri are shown for clarity. White circles denote visible electrodes in the operative view, and gray circles invisible electrodes. Note that the frontal CCEP stimulus site (a black pair of electrodes) corresponded with the anterior language area defined by fMRI in all patients. The right column: The AF tracts (green) were shown in comparison with subdural electrodes.

× 8 grid (Patient 5)] were placed so that the stimulus site (a pair of two adjacent electrodes) became the closest to the AF tract integrated in the neuro-navigation. To define the function of the white matter tract, reading and picture naming tasks were performed when high-frequency ES (50 Hz, 3–5 s, 10–15 mA) was applied to the white matter at the stimulus site. Only the impaired behaviors that were reproducible without afterdischarges in ECoG were adopted as significant. To trace the connection from the subcortical stimulus site to the frontal and temporoparietal cortices, single-pulse ES (1 Hz, 10–15 mA, 2 × 30 trials) were delivered to the stimulus site. SCEPs were recorded from the electrodes on the frontal and temporoparietal cortices. Since a 32-channel intraoperative monitoring system was used, SCEPs and raw ECoG were recorded from the selected electrodes around the frontal stimulus sites and temporoparietal CCEP response sites. The averaging methods of SCEPs were the same as those of CCEPs.

Display and Analysis of CCEP and SCEP

As previously reported [Matsumoto et al., 2004], CCEPs consist of an early (N1) negative potential and a late (N2) negative potential. The N1 peak was visually identified as the first negative deflection that was clearly distinguishable from the stimulus artifacts. The onset, peak latency, and amplitude of N1 were measured as reported previously elsewhere [Matsumoto et al., 2004]. Briefly, a line was drawn from the onset to the offset of the N1 potential for each data point, and the N1 amplitude was measured as the height of a vertical line drawn from the negative peak of N1 to the intersection of the vertical line with the above-described line.

In order to illustrate the distribution of each activity over the cortices, a circle map was employed based on the amplitude percentage distribution, in which the diameter of the circle at each electrode represented the percentile to the maximal amplitude of that particular activity (Fig. 2). Since we had not performed intraoperative MRI, the placement of electrodes was identified based on operative observation and neuro-navigation data.

The CCEP amplitude was continually monitored in comparison with the largest CCEP amplitude recorded at the PL immediately after the patients were awakened. The baseline CCEP amplitude was adopted at this awake condition since general anesthesia could reduce cortical evoked potentials [Howard et al., 2000], and surgical procedures at and around the language cortex and fibers were usually planned during the awake condition.

In order to avoid intraoperative artifacts, CCEPs and SCEPs were also analyzed offline in MATLAB (Mathworks, Inc., Natick, MA) by averaging ECoGs time-locked to the stimulus onset, with a time window of 600 ms (from 100 ms before to 500 ms after the stimulus onset) and a band-pass filter (the same as intraoperative online methods). The baseline was set at 95 ms before stimulus onset.

MRI Data Acquisition Before and After Surgery

MRI scans were performed before and after surgery. Postoperative MRI scans were usually done between 2 and 6 weeks after surgery. Diffusion-weighted images (DWI), fMRI, and a T1 weighted anatomical image were acquired on a 3-Tesla Trio scanner (Siemens, Erlangen, Germany). The parameters of DWI, the T1-weighted image, and the dual gradient field map are reported elsewhere [Oguri et al., 2013]. fMRI was performed only preoperatively by using echo planar imaging in an axial orientation with the following parameters: repetition time = 2,500 ms, echo time = 30 ms, flip angle = 90°, voxel size = 3 mm × 3 mm × 3 mm, field of view = 192 mm × 192 mm, matrix size = 64 × 64, 40 slices.

fMRI Language Task and Data Analysis

The Japanese shiritori word generation task was used. "Shiritori" is a popular Japanese word chain game to generate an appropriate noun that starts with the last kana letter of the noun presented just before it in tandem. For example, when "ringo" (apple) is presented, the patient must generate a noun beginning with the kana letter "go," such as "gorira" (gorilla). The activated brain areas are similar to those activated in Western word generation tasks: the left inferior frontal gyrus (IFG) [including IFGop, IFGtr, and the pars orbitalis (IFGor)], the left superior and middle frontal gyri (MFG), the right IFG, and the right cerebellar hemisphere in right-handed healthy subjects [Inoue et al., 2011].

Patients were instructed to do shiritori silently in the activation block and to fixate on a white crosshair, without any body movements, in the rest block following the visual stimuli through a mirror built into the head coil. Each fMRI session consisted of four activation blocks (30 s each), and five rest blocks (30 s each). Two sessions were performed in each patient.

Functional data were analyzed by FMRIB Software Library (FSL 4.1.6; www.fmrib.ox.ac.uk/fsl) [Smith et al., 2004] and Statistical Parametric Mapping (SPM) 8 (Wellcome Department of Cognitive Neurology, London, UK; www.fil.ion.ucl.ac.uk/spm), as reported elsewhere [Oguri et al., 2013]. Statistical maps comparing the shiritori word generation and rest were calculated at a threshold of $P < 0.001$ (uncorrected).

Diffusion Tractography of the AF

The AF was reconstructed by placing two regions of interest (ROI) in the cerebral deep white matter on a coronal directional color-coded map [Matsumoto et al., 2008; Wakana et al., 2007]. To reconstruct the AF tract, an anterior ROI was identified in the coronal slice at the level of the midpoint of the posterior limb of the internal capsule as a triangle-shaped region where the fibers were running in an anterior–posterior orientation. A posterior ROI was

CCEP waveform at the maximum response site before and after removal

Patient 1
N1
CCEP N1 amplitude
— before removal: 342 μV
— after removal: 368 μV
100 μV
50 ms

Patient 2
— before removal: 500 μV
— after removal: 440 μV
(12% decrease)
100 μV
50 ms

Patient 3
— before removal: 311 μV
— after removal: 329 μV
100 μV
50 ms

Patient 4
— before removal: 383 μV
— after removal: 260 μV
(32% decrease)
100 μV
50 ms

Patient 5
— before removal: 197 μV
— after removal: 227 μV
100 μV
50 ms

Patient 6
— before removal: 230 μV
— after removal: 245 μV
50 μV
50 ms

N1 amplitude
○ 100%
○ 80%-
○ 60%-
○ 40%-   ●● stimulus site
○ 20%-   ○ CCEP response site   ► the maximum CCEP response site   ⊃ arcuate fasciculus
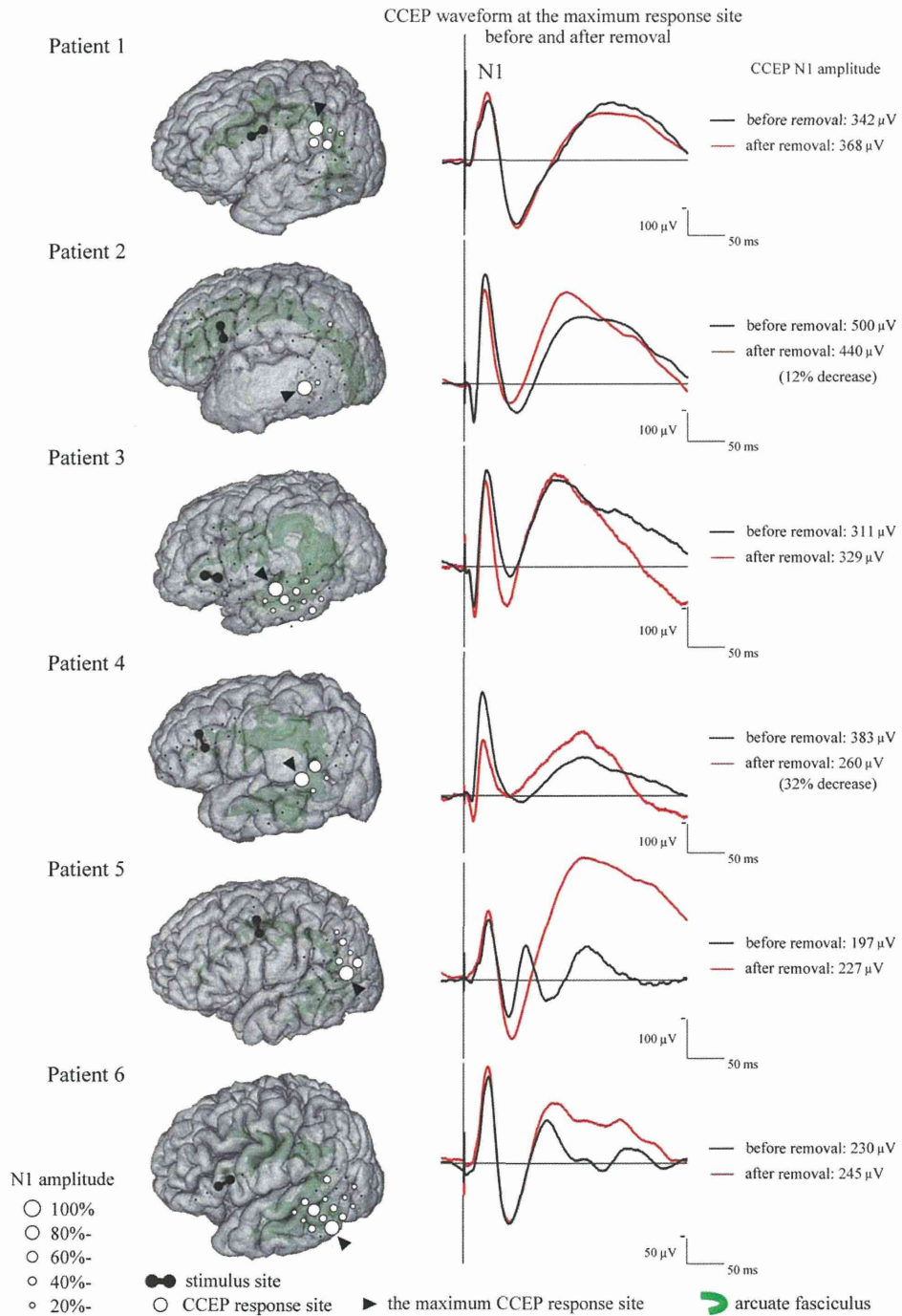
Figure 2.

Behavior of the CCEP N1 amplitude during tumor removal in the awake condition. The left column shows the CCEP distribution with a circle map in each patient in the awake condition. The diameter of the circle at each electrode represented the percentile to the largest amplitude at the maximum CCEP response site. The right column shows the N1 waveform at the maximum CCEP response site in each patient. The black line represents the N1 waveform immediately after the awake condition, and the red line that after tumor removal. A N1 amplitude decrease was noted in Patient 2 (12%) and Patient 4 (32%).

identified in the axial slice at the level of the anterior commissure as a region where the fibers in the superior–inferior orientation were running lateral to the sagittal stratum [Wakana et al., 2007].

Probabilistic diffusion tractography was drawn from the anterior ROI to the posterior ROI by using tools from FSL, as reported elsewhere [Oguri et al., 2013]. To exclude erroneous connections, samples were discarded if they passed into the interhemispheric fissure, thalamus, or ipsilateral peduncle. The threshold of tractography was set to 0.1% of the maximum connectivity value. The connectivity value was the number of samples that pass through the voxel, which was automatically output by the FSL software. This threshold was set lower than in the previous tractography study [Yogarajah et al., 2010], in order to describe the tractography until cortices and to avoid the influence of brain edema caused by the tumor. All the ROI manipulations were performed by one author (Y.Y.) who had sufficient experience with fiber tractography.

Validation of the CCEP/SCEP Stimulus and Response Sites

During the awake condition, language function was confirmed by 50 Hz ES at the stimulus sites for CCEP (the frontal cortex) and SCEP (white matter pathway). In addition, the anatomical locations of the CCEP/SCEP stimulus and response sites were compared with the activation area of fMRI by the shiritori word generation task and with the cortical terminations of the AF tract. We regarded the findings of the invasive and noninvasive tests as consistent when the distance between the stimulus/response site (either electrode between a pair) and either the activation area of fMRI or the cortical termination of the AF tract was within 7 mm, as reported in a previous combined study of CCEP and tractography [Conner et al., 2011]. As for the CCEP/SCEP response site, the electrodes showing >20% of the amplitude of the maximum response were defined as CCEP/SCEP-positive electrodes, and adopted for validation of the findings of the noninvasive test. We regarded the findings of the AF tract and high-frequency ES in the white matter as consistent when the distance between the AF tract and the stimulus site was within 6 mm, as described in a previous study [Kamada et al., 2007].

RESULTS

CCEP Connectivity Pattern Between the Perisylvian Language Areas

In all patients, single-pulse ES was delivered, under general anesthesia, to the candidate cortices for the frontal stimulus site (3–8 sites per patient), according to the preoperative evaluation. As shown in a representative case (Patient 4, Fig. 3), four candidate stimulus sites were stimulated in the left IFGtr and IFGop, and CCEPs were recorded from the 2 × 8 grid placed in the left temporoparietal area. CCEP connectivity was changed considerably by shifting the stimulus site by 1 cm along the rostrocaudal dimension. It was the stimulation at the IFGtr (the electrode pair of B05–13) that elicited the maximum CCEP response (Electrode A04, N1 peak latency of 25.8 ms) in the posterior part of the STG. The candidate stimulus site that showed the maximum CCEP response in the left lateral temporoparietal area with a relatively early N1 peak was defined as the putative AL. This putative AL was then used as the stimulus site for subsequent online CCEP monitoring. In all patients, the CCEP connectivity pattern successfully delineated the frontal stimulus site (the putative AL) and the maximum CCEP response site (the putative PL) for the sequential monitoring of CCEP amplitude (Fig. 2).

The results of CCEP are summarized in Tables II and III. The frontal stimulus site (the electrode pair in the putative AL) was located in the IFGtr in four patients, the IFGop in three, and the most caudal part of the MFG in one. In all patients, the frontal stimulus site was confirmed as the core AL by high-frequency ES; speech arrest was observed in four patients (Patients 1, 4, 5, and 6), and slowing of speech in two (Patients 2 and 3) during the picture naming task. As expected from the results of high-frequency ES, the location of the frontal stimulus site was consistent with that of fMRI activation in all patients and the cortical terminations of the AF tract in five.

Upon AL stimulation, CCEPs were recorded from the posterior part of the STG (six patients), MTG (four patients), and the inferior temporal gyrus (ITG, three patients) in the temporal lobe, as well as the angular and the supramarginal gyri (AG/SMG, three patients) in the parietal lobe (see Table III for N1 latency). In the lateral temporoparietal area, fMRI activation was observed in four patients, and the cortical terminations of the AF tract could be traced into the cortex in all but Patient 2 who had a large tumor and surrounding edema in this area. The distribution of CCEP response sites was consistent with fMRI activation in four patients, and with the cortical terminations of the AF tract in four.

Online CCEP Monitoring and Functional Outcome

Except for two patients in whom the grid was replaced or moved because of clinical necessity when the patients awoke, CCEPs were monitored with the exact same electrode position during both general anesthesia and awake condition (four patients). In these four patients, when the patients woke up, the N1 amplitude increased by an average of 116 μV (ranging from 96 to 139), increased by 60% at the maximum CCEP response site. The CCEP distribution did not change (i.e., did not get wider). As for the N1 latencies, the onset latency changed by an average of 1.0 ms (ranging from −0.8 to 3.3), and the peak latency